

# Bow-shock instability in entry, descent, and landing vehicles under high-enthalpy conditions

Adrián Antón-Álvarez<sup>1,†</sup> and Adrián Lozano-Durán<sup>1,2</sup>

<sup>1</sup>*Graduate Aerospace Laboratories, California Institute of Technology, Pasadena, CA 91125, USA*

<sup>2</sup>*Department of Aeronautics and Astronautics,  
Massachusetts Institute of Technology, Cambridge, MA 02139, USA and*

<sup>†</sup>Corresponding author: aantonal@caltech.edu

Laminar–turbulent transition remains a major uncertainty in the aerothermal design of entry, descent, and landing (EDL) vehicles. We show that, under high-enthalpy Mars-entry conditions, the detached bow shock and the shock-generated shear–entropy layer can become unstable under freestream disturbances, leading to nonlinear breakdown and enhanced wall heating. The analysis is carried out at high altitude with freestream Mach numbers ( $M_\infty$ ) up to 30 for both Earth and Mars, with the latter being more susceptible to this instability. The freestream receptivity analysis shows that disturbance amplification occurs through a three-step mechanism: (i) transmission and amplification of acoustic and entropic freestream components across the bow shock; (ii) further convective amplification within the post-shock shear–entropy layer; and (iii) bow-shock corrugation driven by the downstream pressure field, which reinforces the instability. The dominant response is localized in the shock layer, and no classical boundary-layer mode is required to explain the disturbance amplification. The total optimal energy gain scales as  $\overline{G}_T^{\text{opt}} \sim \gamma_2^* M_\infty^2 \exp[(\rho_2/\rho_1)/C - B/\sqrt{Re_\infty}]$ , where  $\gamma_2^*$  is an effective specific-heat ratio,  $\rho_1$  and  $\rho_2$  are the pre- and post-shock densities,  $Re_\infty$  is the freestream Reynolds number, and  $B$  and  $C$  are geometry-dependent constants. For a representative EDL vehicle during Mars entry, the resulting amplification factors are of order  $10^6$ . We further show that flight measurements from the Mars Science Laboratory (MSL) and Mars 2020/Perseverance capsules [1, 2] are consistent with these results. The findings are also supported by wall-modeled large-eddy simulations of MSL under representative Mars-entry conditions. These results suggest that bow-shock instabilities may constitute a transition mechanism for blunt hypersonic entry vehicles, either as a standalone process or in combination with others.

Keywords: hypersonics, bow shock, stability analysis, freestream receptivity

## I. INTRODUCTION

Accurate prediction of laminar-to-turbulent boundary-layer transition remains a fundamental challenge in the design of hypersonic vehicles [3]. The state of the boundary layer directly governs key aerodynamic forces and thermal loads, which are critical for assessing the operational and survival margins of the vehicle. In the turbulent regime, boundary layers produce substantially higher skin friction and, more importantly, significantly increased aerodynamic heating compared to their laminar counterparts [4, 5]. These intensified thermal loads impose stringent requirements on the thermal protection system (TPS) design, affect-

ing vehicle mass budgets, mission payload fractions, and structural durability. Inaccurate prediction of these forces and thermal loads can lead either to overly conservative designs with excessive weight penalties or to optimistic designs that are vulnerable to thermal failure. The Mars Science Laboratory (MSL) and Mars 2020/Perseverance entry, descent, and landing (EDL) missions exemplify these challenges, with reconstructed flight aeroheating data indicating transition and associated elevated heating during entry [1, 2, 6].

The transition characteristics of MSL were experimentally studied through campaigns spanning multiple hypersonic test facilities [5, 7–9]. Those ground-test data showed transition and turbulent-heating augmentation preferentially on the leeside of the capsule rather than on the windside. The associated leeside heat-flux augmentation became a critical consideration in sizing the TPS. During the actual MSL mission, post-flight heat-flux data were reconstructed, indicating elevated heating on the leeside consistent with transition [1]. Similar leeside heating behavior was subsequently documented for the Perseverance mission [2, 6], suggesting a recurring trend for MSL-class Mars entry capsules and underscoring the importance of understanding the underlying mechanisms for future mission design.

Drawing on the database of experimental measurements, Hollis [5] proposed an empirical criterion for smooth blunt-body transition onset based on the momentum-thickness Reynolds number, approximately  $Re_\theta \approx 200$ . However, the numerical simulations used during the MSL design phase with the steady-state LAURA solver were generally restricted to operating in either fully laminar or fully turbulent mode [10, 11]. While these simulations successfully estimated the expected range of wall heating and reproduced observed transition locations when appropriately tuned, they lack inherent predictive capability regarding the physical mechanisms that trigger transition or the conditions governing its onset and location. This limitation represents a significant gap in the theory required for extrapolation to realistic flight conditions, which cannot be fully reproduced experimentally on Earth.

The present work addresses the following question: in high-enthalpy hypersonic flow over blunt bodies, can freestream disturbances be amplified through interactions between the bow shock and the shear–entropy layer before conventional boundary-layer instabilities become dominant?

### A. Freestream receptivity

Experimental evidence has long indicated that transition in high-speed regimes is strongly influenced by both the structure and intensity of freestream disturbances [12, 13], making receptivity theory a central link between environmental disturbances and the onset of transition over hypersonic vehicles.

Early theoretical investigations employed linear interaction analysis (LIA) to derive analytical scaling laws for infinitesimal disturbance amplification across normal and oblique shock waves. In the strong-shock limit, McKenzie and Westphal [14] showed that the pressure amplitude and the shock-normal wave-energy flux associated with transmitted acoustic/entropic perturbations scale as  $O(M_\infty^2)$ . For incident vortical disturbances, classical LIA predicts more modest amplification of the post-shock vortical (kinetic-energy-containing) fluctuations, with gains that depend on shock strength and incidence [15]. This qualitative picture is consistent with later numerical studies of shock/turbulence interaction [16]. A key implication of LIA is that, because the shock jump conditions couple thermodynamic and velocity perturbations, a single upstream Kovásznyai mode (acoustic, vortical, or entropic) typically generates all

three modes downstream, providing multiple pathways for post-shock base-flow excitation.

Once disturbances are transmitted and amplified across the bow shock, receptivity studies have shown that coupling between Mack modes and slow acoustic perturbations often dominates the receptivity process in canonical high-speed boundary layers on flat plates, wedges, and slender bodies. Fedorov and Khokhlov [17] and Fedorov [18] applied the Kovásznyai decomposition to analyze post-shock disturbance fields and demonstrated that slow acoustic modes can synchronize with Mack’s second mode, i.e., a resonance-like matching of phase speeds that enables sustained forcing of the instability by the slow acoustic wave. This synchronization facilitates efficient energy transfer from freestream disturbances to modal instabilities. Ma and Zhong [19, 20] extended receptivity theory by identifying intermediate modes that bridge freestream acoustic forcing and boundary-layer instabilities. Although these modes are stable, they are excited preferentially and subsequently transfer energy to the unstable second mode via slow-acoustic synchronization, enabled by phase-speed matching and spatial overlap. In this view, the shock does more than amplify incoming disturbances: it organizes the post-shock disturbance field in a way that promotes efficient coupling into the dominant instability waves. Building on this perspective, Qin and Wu [21] uncovered a continuous resonance process in which slow acoustic modes repeatedly reflect between the shock and the wall, leading to a persistent excitation mechanism that is intrinsic to shock-bounded flows and has no analogue in shock-free configurations. Motivated by these observations, more recent work has sought to capture the global interaction of shock transmission, reflection, and instability development within unified receptivity frameworks. For example, Kamal *et al.* [22] developed a global receptivity approach with realizable excitations of acoustic, entropic, and vortical disturbances, offering a detailed description of how freestream fluctuations penetrate and couple into the boundary layer across the entire flow field.

## B. Current challenges and limitations

In this work, we address challenges and limitations that arise when the studies surveyed above are viewed in the context of hypersonic EDL vehicles under flight-relevant conditions.

- *Stability and receptivity mechanisms specific to EDL vehicles.* Many hypersonic transition studies have focused on slender configurations (e.g., HiFiRE-type cones), where Mack-mode dynamics are a central mechanism [3]. Blunt entry capsules, however, exhibit a fundamentally different flow topology: a strong, detached bow shock produces substantial deceleration and thermodynamic changes, yielding post-shock edge Mach numbers that are often subsonic or only weakly supersonic over much of the forebody. Moreover, bow-shock curvature and shock-layer non-parallelism can introduce global coupling effects that are absent in canonical slender-body settings. As a result, the instability mechanisms governing EDL vehicles may differ from those of slender bodies, and their characterization remains less well established. These differences extend to receptivity, where prior work has largely emphasized the excitation of Mack-mode instabilities by freestream disturbances on cone-like bodies. Here, we perform receptivity analyses tailored to EDL-vehicle-like flows, explicitly accounting for bow-shock curvature and shock-layer non-parallelism.
- *High-enthalpy, realistic flight conditions.* A large fraction of the available computational and experimental literature focuses on low-enthalpy conditions under calorically

perfect-gas assumptions. Realistic EDL trajectories, however, involve high enthalpy, thermochemical effects, and freestream Mach numbers approaching  $M_\infty \approx 30$ . These effects modify the base flow (shock-layer structure, temperature, and composition profiles) and the disturbance dynamics (acoustic propagation, entropic production, and mode coupling), limiting the direct applicability of low-enthalpy insights. In our analysis, we account for thermochemical effects at flight-relevant Mach numbers using an equilibrium model to better quantify these sensitivities.

- *Experimental limitations.* The disturbance levels in ground-based experiments can differ markedly from those in atmospheric flight. In conventional hypersonic tunnels, acoustic radiation from turbulent boundary layers on the tunnel walls often constitutes a dominant source of freestream forcing, with levels that can exceed those in flight by orders of magnitude [23]. Many of the experiments used to support the MSL design were conducted in such non-quiet facilities [5, 7–9, 11]. This facility-specific disturbance environment raises questions about how directly tunnel-based transition trends and criteria translate to free flight, where freestream acoustic levels are expected to be substantially lower. Complicating this comparison further, entry trajectories typically involve freestream Mach numbers well above those achievable in many tunnels, while the tunnel acoustic amplitudes are often higher. Hence, we consider flight-relevant conditions to better assess the conclusions from tunnel-to-flight extrapolations.

The remainder of the paper is organized as follows. Section II presents the theoretical and computational methodology. Section III A examines the receptivity of the shock layer to freestream disturbances, and §III B analyses the energy budgets of the resulting optimal disturbance. Section III C develops scaling laws for the identified optimal response, §III D examines the feedback associated with shock corrugation, and §III E maps the resulting gain over velocity–altitude space for Mars and Earth entry conditions. Finally, §III F investigates the nonlinear instability dynamics using wall-modeled large-eddy simulation.

## II. METHODS

### A. Problem setup

We consider flow over a simplified axisymmetric capsule intended to isolate the forebody shock-layer dynamics relevant to blunt EDL vehicles. The geometry consists of a spherical nose cap of radius  $R$  that blends smoothly into a conical frustum of half-angle  $\theta = 52.7^\circ$ , as shown in figure 1. The spherical and conical portions meet tangentially. The value  $\theta = 52.7^\circ$  is chosen as an effective half-angle,  $\theta = 70^\circ - \alpha$ , so that the axisymmetric configuration approximates the leeside inclination of the MSL  $70^\circ$  sphere-cone at the representative flight angle of attack  $\alpha = 17.3^\circ$ .

A Cartesian reference frame is adopted in the meridional plane. The  $x$ -axis is aligned with both the freestream direction and the axis of symmetry of the body. The origin is located at the nose apex. For the axisymmetric zero-angle-of-attack base flow considered here, this point is also the wall stagnation point. The coordinate  $y$  denotes the radial direction in the meridional plane.

The freestream state is specified by the density  $\rho_\infty$ , velocity  $U_\infty$ , temperature  $T_\infty$ , and species mole fractions  $X_i$ , resulting in the freestream composition  $\mathbf{X}_\infty$ . Table I lists the repre-

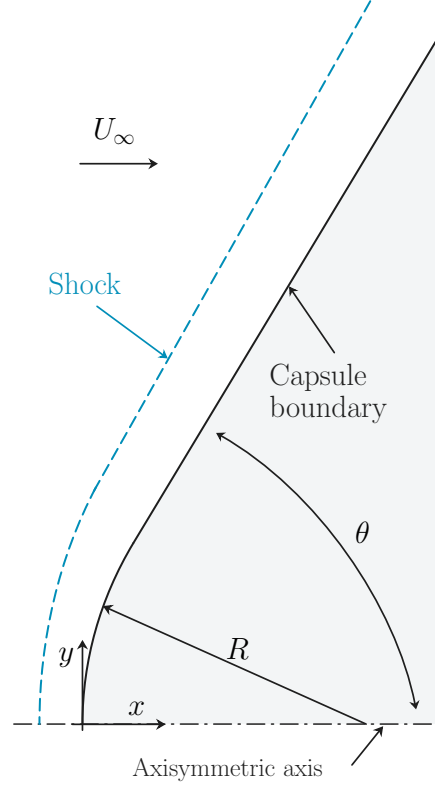


FIG. 1: Reference coordinate system and geometric notation for the simplified capsule.

$U_\infty$ [m/s]	$\rho_\infty$ [kg/m <sup>3</sup> ]	$T_\infty$ [K]	Freestream composition	$M_\infty$
5 690	0.000351	158	$X_{\text{CO}_2} : 0.9556, X_{\text{N}_2} : 0.0270, X_{\text{Ar}} : 0.0160, X_{\text{O}_2} : 0.0014$	28.7

TABLE I: Representative Mars-entry baseline used to define the reference configuration. The species mole fractions  $X_i$  correspond to the Martian atmosphere.

sentative Mars-entry baseline used to define the reference configuration. This state is selected because it lies near the velocity–altitude region of the MSL and Mars 2020/Perseverance entries where reconstructed aeroheating data indicate enhanced leeside heating associated with transition [1, 2, 6]. Additional freestream states used in the Reynolds-number, Mach-number and trajectory sweeps are introduced in §III C and §III E. For the class of conditions considered here, a detached bow shock forms ahead of the nose. The shock standoff distance, post-shock thermochemical state and shock-layer gradients determine the stability and receptivity properties analyzed below.

## B. Modeling equations

### 1. Compressible Navier–Stokes equations

The flow is modeled as a continuum, viscous, heat-conducting, single-temperature equilibrium gas mixture. Unless otherwise stated, length, velocity, density, pressure, and time are non-dimensionalized by  $R$ ,  $U_\infty$ ,  $\rho_\infty$ ,  $\rho_\infty U_\infty^2$  and  $R/U_\infty$ , respectively. The specific internal energy is non-dimensionalized by  $U_\infty^2$ , the temperature by  $U_\infty^2/c_{v\infty}$ , and the entropy by  $c_{v\infty}$ . With these conventions, the governing equations are

$$\frac{\partial \rho}{\partial t} + \frac{\partial(\rho u_i)}{\partial x_i} = 0, \quad (1a)$$

$$\frac{\partial(\rho u_i)}{\partial t} + \frac{\partial(\rho u_i u_j)}{\partial x_j} = -\frac{\partial[(\gamma^* - 1)\rho e]}{\partial x_i} + \frac{\partial \tau_{ij}}{\partial x_j}, \quad (1b)$$

$$\frac{\partial(\frac{1}{2}\rho u_i u_i + \rho e)}{\partial t} + \frac{\partial[(\frac{1}{2}\rho u_i u_i + \gamma^* \rho e) u_j]}{\partial x_j} = \frac{\partial(\tau_{ij} u_i)}{\partial x_j} - \frac{\partial q_i}{\partial x_i}, \quad (1c)$$

$$\tau_{ij} = \frac{\mu^*}{Re_\infty} \left( \frac{\partial u_j}{\partial x_i} + \frac{\partial u_i}{\partial x_j} - \frac{2}{3} \frac{\partial u_k}{\partial x_k} \delta_{ij} \right), \quad (1d)$$

$$q_i = -\frac{\gamma_\infty k^*}{Re_\infty Pr_\infty} \frac{\partial}{\partial x_i} \left( \frac{e}{c_v^*} \right). \quad (1e)$$

Here  $u_i$  are the velocity components,  $\rho$  is the density,  $e$  is the specific internal energy,  $p$  is the pressure,  $T$  is the temperature,  $\tau_{ij}$  is the viscous stress and  $q_i$  is the heat flux. The effective thermodynamic quantities are  $\gamma^* = 1 + p/(\rho e)$  and  $c_v^* = e/T$ , while the non-dimensional transport coefficients are  $\mu^* = \mu/\mu_\infty$  and  $k^* = k/k_\infty$ . The corresponding non-dimensional groups are

$$Re_\infty = \frac{\rho_\infty U_\infty R}{\mu_\infty}, \quad \gamma_\infty = \frac{c_{p\infty}}{c_{v\infty}}, \quad Pr_\infty = \frac{\mu_\infty c_{p\infty}}{k_\infty}, \quad (2)$$

where  $c_{p\infty}$  is the freestream specific heat at constant pressure. The thermochemical models for  $\gamma^*$  and  $c_v^*$  along with the transport models for  $k^*$  and  $\mu^*$  are discussed in the next section. The governing equations are closed with the ideal-mixture equation of state

$$p = \rho R_g T,$$

where the local mixture gas constant  $R_g$  is non-dimensionalized by  $c_{v\infty}$ .

The use of the continuum equations is justified by the small body-scale Knudsen number:

$$Kn_\infty \simeq \sqrt{\frac{\pi \gamma_\infty}{2}} \frac{M_\infty}{Re_\infty}.$$

At the freestream state in table I, this estimate gives  $Kn_\infty \simeq 4 \times 10^{-4}$  for  $Re_\infty = 10^5$ . Additionally, the local Knudsen number is even smaller in the compressed post-shock region. Therefore, the flow is well within the continuum regime at the body scale relevant to the present analyses.

## 2. Thermochemical and transport models

High-enthalpy Mars-entry conditions require a thermochemical model that accounts for the redistribution of internal energy among translational, rotational, vibrational, and chemical modes. Vibrational excitation and finite-rate chemistry, particularly dissociation at sufficiently high temperature, can alter the shock standoff distance, density ratio, temperature field and entropy gradients that control the stability of the shock layer.

We assume a chemically and thermally equilibrated ideal-gas mixture for both the base-flow calculations and the receptivity analysis. Under this assumption, separate species-transport and vibrational-energy equations are not solved. Instead, the local composition is obtained algebraically from the equilibrium relations. The constitutive models for

$$\gamma^* = \gamma^*(\rho, e; \mathbf{X}_\infty), \quad c_v^* = c_v^*(\rho, e; \mathbf{X}_\infty), \quad \mu^* = \mu^*(\rho, e; \mathbf{X}_\infty), \quad k^* = k^*(\rho, e; \mathbf{X}_\infty)$$

are described in [24]. The equilibrium thermochemical model also provides  $R_g$ , the local equilibrium composition, and the local speed of sound.

The validity of the equilibrium assumption is assessed in Appendix A. For reference, we define the chemical and vibrational Damköhler numbers using the body-scale post-shock flow time  $\tau_{\text{flow}} = R/U_2^{\text{RH}}$ , where  $U_2^{\text{RH}}$  is the post-shock normal velocity from the corresponding normal-shock Rankine–Hugoniot estimate. Thus

$$Da_{\text{chem}} = \frac{\tau_{\text{flow}}}{\tau_{\text{chem}}}, \quad Da_{\text{vib}} = \frac{\tau_{\text{flow}}}{\tau_{\text{vib}}}. \quad (3)$$

For the baseline Mars-entry state, Appendix A gives  $Da_{\text{chem}} = O(10^2)$ – $O(10^3)$  and  $Da_{\text{vib}} = O(10^4)$ – $O(10^5)$  in the critical velocity–altitude region. The relaxation times are therefore short relative to the residence time of the gas in the forebody shock layer, supporting the use of an equilibrium model for the stability calculations reported here. The equilibrium calculations and the relaxation-time estimates are obtained with Cantera [25], as described in Appendix A.

The mixture transport coefficients,  $\mu^* = \mu^*(\rho, e; \mathbf{X}_\infty)$  and  $k^* = k^*(\rho, e; \mathbf{X}_\infty)$ , are evaluated using standard mixture rules: Wilke’s formula for viscosity [26] and the Mason–Saxena relation for thermal conductivity [27]. Species diffusion and diffusive enthalpy transport are neglected in the present equilibrium-mixture formulation.

## 3. Boundary conditions

Boundary conditions are imposed at the fitted bow shock, the capsule surface, the symmetry axis and the downstream outflow plane.

- *Bow shock.* Only the post-shock region is discretized. For the steady base flow, the state immediately downstream of the fitted shock satisfies the Rankine–Hugoniot jump relations with the uniform freestream, closed by the equilibrium-mixture thermodynamic model. In the linearized calculations, the jump relations and the shock kinematic condition are linearized about the fitted-shock base state, so that shock displacement and post-shock perturbations are coupled consistently.

- *Wall.* No-slip and adiabatic-wall conditions are imposed at the capsule surface,

$$\mathbf{u} = \mathbf{0}, \quad q_j n_j = 0,$$

where  $\mathbf{n}$  is the unit normal to the wall. This is a deliberate simplification relative to a flight heat shield, for which wall cooling, catalysis, ablation, pyrolysis and radiation may affect the near-wall thermal state. The dominant linear responses identified below are localized primarily in the outer shock layer. Additional calculations with cooled-wall conditions produced the same shock-layer amplification mechanism.

- *Axis of symmetry.* Symmetry conditions are imposed along the geometric symmetry axis.
- *Outflow.* Non-reflecting characteristic conditions are applied at the downstream boundary following Poinot and Lele [28].

### C. Numerical solver

The computations are performed with the Hypersonic Linear Stability Toolkit (HYMOR), an open-source solver for global modal, non-modal and receptivity analyses of hypersonic shock layers [24]. Only the key information needed for the present study is summarized here.

The receptivity calculations reported in §III are axisymmetric: the base flow and perturbations are represented in the meridional plane and no azimuthal modes are included. HYMOR solves the axisymmetric compressible Navier–Stokes equations with a second-order cell-centered finite-volume method on a body-fitted curvilinear grid. Cell-centered states are linearly interpolated to face midpoints, face integrals are evaluated with midpoint quadrature and time integration of the nonlinear base flow uses the classical four-stage fourth-order Runge–Kutta scheme.

The bow shock is treated by shock fitting rather than shock capturing. The fitted shock is represented by a cubic spline whose degrees of freedom evolve with the shock kinematic condition. The discontinuity is therefore imposed as a boundary condition of the computational domain. This avoids shock-capturing pathologies such as the carbuncle phenomenon [29] and, more importantly for the present study, retains the linear coupling between infinitesimal shock motion and the post-shock perturbation field. In the linearized solver, the Rankine–Hugoniot relations, shock kinematics and interior finite-volume residual are differentiated consistently about the shock-fitted base state.

Computations were performed on three progressively refined meshes, denoted coarse, base and fine. At the representative condition  $Re_\infty = 285\,000$ , these meshes contain  $1000 \times 160$ ,  $2000 \times 320$  and  $4000 \times 640$  control volumes in the streamwise and wall-normal directions, respectively. The grid is clustered near the wall, across the post-shock shear–entropy layer and near the fitted shock. A systematic refinement study confirmed that the leading long-time optimal gain differs by less than 3% between the base and fine meshes. The base mesh is therefore used for the results reported below.

### 1. Freestream receptivity

We use non-bold symbols for continuous fields and bold symbols for discrete vectors and matrices. The continuous conservative flow state is

$$\mathbf{q} = [\rho, \rho u, \rho v, \rho E]^T, \quad E = e + \frac{1}{2}u_i u_i,$$

where  $u$  and  $v$  are the meridional velocity components. The freestream state is denoted by  $q_\infty$ , while the flow conditions after the shock are given by  $q$ . The total upstream and post-shock fields are decomposed as

$$\begin{bmatrix} q_\infty \\ q \end{bmatrix} = \begin{bmatrix} q_{\infty,0} + q'_\infty \\ q_0 + q' \end{bmatrix}, \quad (4)$$

where the subscript 0 denotes the steady base state and primes denote infinitesimal perturbations.

Because the bow shock is fitted, the discrete perturbation state contains both the post-shock flow perturbations and the displacement of the fitted shock. We write the extended post-shock disturbance as

$$\mathbf{q}'_e = \begin{bmatrix} \mathbf{q}' \\ \boldsymbol{\eta}' \end{bmatrix}, \quad (5)$$

where  $\mathbf{q}'$  contains the cell-centered conservative perturbation variables and  $\boldsymbol{\eta}'$  contains the perturbations of the shock-spline degrees of freedom. The freestream receptivity problem is posed as an input–output problem: a prescribed perturbation immediately upstream of the fitted shock interacts with the Rankine–Hugoniot boundary conditions and forces the post-shock response. The post-shock perturbation is initially zero.

Linearization about the steady shock-fitted base state  $\mathbf{q}_{e,0}$  gives the semi-discrete forced system

$$\frac{d\mathbf{q}'_e}{dt} = \mathbf{L}(\mathbf{q}_{e,0})\mathbf{q}'_e + \mathbf{B}\mathbf{q}'_\infty(t), \quad \mathbf{L}(\mathbf{q}_{e,0}) \equiv \left. \frac{\delta \mathbf{N}}{\delta \mathbf{q}_e} \right|_{\mathbf{q}_{e,0}}. \quad (6)$$

Here  $\mathbf{N}$  is the nonlinear shock-fitted residual, including the interior finite-volume equations, the shock kinematic condition and the Rankine–Hugoniot compatibility conditions. The matrix  $\mathbf{L}$  is evaluated numerically by finite differences and is written simply as  $\mathbf{L}$  hereafter. The vector  $\mathbf{q}'_\infty(t)$  denotes the discrete freestream perturbation of the conservative variables immediately upstream of the shock points,

$$\mathbf{q}'_\infty = [\boldsymbol{\rho}'_\infty, (\boldsymbol{\rho}\mathbf{u})'_\infty, (\boldsymbol{\rho}\mathbf{v})'_\infty, (\boldsymbol{\rho}\mathbf{E})'_\infty]^T. \quad (7)$$

The coupling matrix  $\mathbf{B}$  is the linearized map from this upstream shock trace to the post-shock residual. This finite-difference construction automatically includes the linearized response of the shock-fitting boundary treatment and the Rankine–Hugoniot jump conditions.

The freestream input is represented only through its trace on the upstream side of the fitted shock. The imposed upstream disturbance is expanded as a finite sum of harmonic

components,

$$\mathbf{q}'_{\infty}(s, t) = \Re \left\{ \sum_{l=0}^{N_{\omega}} \widehat{\mathbf{q}}'_{\infty, l}(s) \exp(-i\omega_l t) \right\}, \quad (8)$$

where  $s$  denotes the arc length along the shock surface and the temporal frequencies  $\omega_l$  are specified by the user. The actual optimization is performed for the disturbance over the bow shock through the functions  $\widehat{\mathbf{q}}'_{\infty, l}(s)$  in (8). After discretization of the shock surface, each complex amplitude  $\widehat{\mathbf{q}}'_{\infty, l}$  contains the conservative-variable perturbations at the shock points for the  $l$ th frequency. The frequency blocks satisfy

$$\frac{d\widehat{\mathbf{q}}'_{\infty, l}}{dt} = -i\omega_l \widehat{\mathbf{q}}'_{\infty, l}, \quad \mathbf{q}'_{\infty}(t) = \sum_{l=0}^{N_{\omega}} \widehat{\mathbf{q}}'_{\infty, l}(t). \quad (9)$$

Thus, after discretization, the unknowns are the complex amplitude values of  $\widehat{\mathbf{q}}'_{\infty, l}(s)$  at the shock points for the selected set of temporal frequencies. No upstream flow field is solved for, and the computation does not require any prescribed relation between temporal frequency and wavenumber. The relevant dispersion relations are introduced only afterward, as an external interpretation of the shock trace, in which the projection of the incident disturbance onto Kovásznyai modes is evaluated *a posteriori*, see Appendix D. This makes it possible to determine the admissible freestream modes—vortical, entropic, and acoustic—excited by the optimal disturbance [22].

Combining (6) and (9) gives a time-dependent input–output problem for the post-shock disturbance. We first collect the initial complex amplitudes of all retained freestream frequencies into the vector

$$\widehat{\mathbf{q}}'_{\infty}(0) = \begin{bmatrix} \widehat{\mathbf{q}}'_{\infty, 0}(0) \\ \widehat{\mathbf{q}}'_{\infty, 1}(0) \\ \vdots \\ \widehat{\mathbf{q}}'_{\infty, N_{\omega}}(0) \end{bmatrix}. \quad (10)$$

Let  $\mathbf{\Omega}$  and  $\mathbf{\Sigma}$  be the operators defined by

$$[\mathbf{\Omega}\widehat{\mathbf{q}}'_{\infty}]_l = \omega_l \widehat{\mathbf{q}}'_{\infty, l}, \quad \mathbf{\Sigma}\widehat{\mathbf{q}}'_{\infty} = \sum_{l=0}^{N_{\omega}} \widehat{\mathbf{q}}'_{\infty, l}, \quad (11)$$

where  $[\cdot]_l$  denotes the block associated with the frequency  $\omega_l$ . Thus,  $\mathbf{\Omega}$  applies the prescribed temporal frequency to each harmonic block, and  $\mathbf{\Sigma}$  sums the frequency blocks to recover the instantaneous upstream perturbation at the shock. Consequently,

$$\widehat{\mathbf{q}}'_{\infty}(t) = \exp(-i\mathbf{\Omega}t)\widehat{\mathbf{q}}'_{\infty}(0), \quad \mathbf{q}'_{\infty}(t) = \mathbf{\Sigma} \exp(-i\mathbf{\Omega}t)\widehat{\mathbf{q}}'_{\infty}(0). \quad (12)$$

Substitution into (6) yields the forced post-shock system

$$\frac{d\mathbf{q}'_e}{dt} = \mathbf{L}\mathbf{q}'_e + \mathbf{F}(t)\widehat{\mathbf{q}}'_{\infty}(0), \quad \mathbf{F}(t) = \mathbf{B}\mathbf{\Sigma} \exp(-i\mathbf{\Omega}t), \quad \mathbf{q}'_e(0) = \mathbf{0}. \quad (13)$$

The corresponding response operator is

$$\mathbf{q}'_e(t) = \int_0^t \exp[\mathbf{L}(t - \tau)] \mathbf{F}(\tau) d\tau \hat{\mathbf{q}}'_\infty(0) \equiv \mathbf{R}(t) \hat{\mathbf{q}}'_\infty(0). \quad (14)$$

Therefore, the downstream response is obtained through the linear input–output map  $\mathbf{R}(t)$ .

The downstream response is measured with Chu’s disturbance-energy norm,

$$E(t) = \int_{V_D} \left[ \underbrace{\frac{\rho_0 a_0^2}{2(\gamma_0^* p_0)^2} p'^2}_{\text{pressure}} + \underbrace{\frac{\rho_0}{2} u'_i u'_i}_{\text{kinetic}} + \underbrace{\frac{(\gamma_0^* - 1) p_0}{2\gamma_0^*} \left( \frac{s'}{R_{g,0}} \right)^2}_{\text{entropic}} \right] dV, \quad (15)$$

where  $V_D$  is the post-shock domain,  $a_0$  is the base-flow speed of sound,  $R_{g,0}$  is the base-flow gas constant and  $s'$  is the entropy perturbation. In discrete form, we obtain

$$E(t) = \mathbf{q}'_e(t)^\dagger \mathbf{P}^\dagger \mathbf{Q}^\dagger \mathbf{M} \mathbf{Q} \mathbf{P} \mathbf{q}'_e(t), \quad (16)$$

where  $\mathbf{P}$  extracts the flow perturbation components from  $\mathbf{q}'_e$  excluding any shock-displacement degrees of freedom,  $\mathbf{Q}$  maps conservative perturbations to Chu variables and  $\mathbf{M}$  contains the quadrature and thermodynamic weights over the post-shock control volumes. The dagger denotes the Hermitian transpose.

The incident input energy is defined from the Chu-energy flux of the prescribed freestream disturbance through the fitted shock. Let  $\mathcal{E}_\infty$  denote the freestream version of the energy density in (15). The instantaneous incident energy flux is

$$\dot{E}_\infty(t) = \int_{S_s} \mathcal{E}_\infty(t) U_\infty |\mathbf{e}_x \cdot \mathbf{n}_s| dS, \quad (17)$$

where  $S_s$  is the fitted-shock surface,  $\mathbf{n}_s$  is the shock normal and  $\mathbf{e}_x$  is the unit vector in the freestream direction. The reference input energy is

$$E_\infty^{\text{ref}} = \overline{\dot{E}_\infty} T^{\text{ref}}, \quad T^{\text{ref}} = \frac{m_D}{\dot{m}_\infty}, \quad (18)$$

where the overbar denotes averaging over the harmonic input,  $m_D = \int_{V_D} \rho_0 dV$  is the base-flow mass contained in the post-shock domain, and

$$\dot{m}_\infty = \int_{S_s} \rho_\infty U_\infty |\mathbf{e}_x \cdot \mathbf{n}_s| dS \quad (19)$$

is the freestream mass flux through the fitted shock. Thus  $T^{\text{ref}}$  is the time required for the base-flow mass flux entering through the shock to replenish the mass contained in  $V_D$ . Then

$$E_\infty^{\text{ref}} = \hat{\mathbf{q}}'_\infty(0)^\dagger \mathbf{D}_\infty \hat{\mathbf{q}}'_\infty(0), \quad (20)$$

where the Hermitian matrix  $\mathbf{D}_\infty$  is described in Antón-Álvarez and Lozano-Durán [24].

The total gain produced by a specified freestream input at time  $t$  is

$$G_T(t) = \frac{E(t)}{E_\infty^{\text{ref}}}. \quad (21)$$

Using (14), this gain can be written as the generalized Rayleigh quotient

$$G_T(t) = \frac{\hat{\mathbf{q}}'_\infty(0)^\dagger \mathbf{C}_\infty(t) \hat{\mathbf{q}}'_\infty(0)}{\hat{\mathbf{q}}'_\infty(0)^\dagger \mathbf{D}_\infty \hat{\mathbf{q}}'_\infty(0)}, \quad (22)$$

where

$$\mathbf{C}_\infty(t) = \mathbf{R}(t)^\dagger \mathbf{P}^\dagger \mathbf{Q}^\dagger \mathbf{M} \mathbf{Q} \mathbf{P} \mathbf{R}(t). \quad (23)$$

The optimal freestream disturbance for the prescribed horizon  $t$  is the leading generalized eigenvector of

$$\mathbf{C}_\infty(t) \hat{\mathbf{q}}'_\infty(0) = G_T(t) \mathbf{D}_\infty \hat{\mathbf{q}}'_\infty(0). \quad (24)$$

The matrix  $\mathbf{C}_\infty(t)$  is not formed explicitly. Its action is evaluated in matrix-free form by applying the forward and adjoint input–output maps associated with (13) and (14). In the implementation, this action is computed using the equivalent autonomous harmonic-forcing operator and the same Taylor-series approximation of the matrix exponential employed in the transient-growth calculation. The Hermitian generalized eigenvalue problem is solved with a Lanczos iteration.

For the frequency sets used below, the forcing produces a periodic response after the initial transient has decayed, provided the unforced post-shock linearized operator is stable. Once an optimal input  $\hat{\mathbf{q}}_\infty^{\text{opt}}(0)$  has been obtained from (24), the instantaneous gain is evaluated from (21). The cycle-averaged gain reported below is

$$\bar{G}_T^{\text{opt}} = \frac{1}{T_p} \int_{t_0}^{t_0+T_p} G_T(t; \hat{\mathbf{q}}_\infty^{\text{opt}}(0)) dt, \quad (25)$$

where  $T_p$  is the forcing period and  $t_0$  is chosen after transients have decayed. The maximum-over-phase gain is

$$G_{T,\text{max}}^{\text{opt}} = \max_{t \in [t_0, t_0+T_p]} G_T(t; \hat{\mathbf{q}}_\infty^{\text{opt}}(0)). \quad (26)$$

These quantities are postprocessed from the optimal freestream forcing mode obtained from the fixed-time eigenproblem (24).

### III. RESULTS

The results are organized as follows. Section III A identifies the leading freestream-receptivity response and decomposes its amplification into shock-transmission and post-shock contributions. Section III B examines the Chu-energy budgets of that response. Section III C develops scaling laws for the shock and downstream gains, and §III D estimates the finite-amplitude feedback associated with bow-shock corrugation. Section III E maps the resulting gain over velocity–altitude space for Mars and Earth entry conditions. Finally, §III F uses wall-modeled large-eddy simulation of the MSL configuration to assess whether the mechanism identified by the linear analysis can lead to nonlinear breakdown.

Mode	$\overline{G}_S^{\text{opt}}$	$\overline{G}_D^{\text{opt}}$	$\overline{G}_T^{\text{opt}}$
1	422	1870	790 000
2	445	951	423 000
3	465	692	322 000
4	489	630	308 000
5	533	386	206 000

TABLE II: Cycle-averaged decomposition of the gain into shock-transmission and downstream-amplification contributions for the five leading optimal freestream forcing modes at  $Re_\infty = 285\,000$  and  $M_\infty = 28.7$ .

### A. Optimal disturbance

We first consider the steady base flow obtained with the freestream conditions listed in table I at  $Re_\infty = 285\,000$ . The corresponding fields are shown in figure 2. A salient feature of this case is the small shock standoff distance: the computed post-shock density exceeds the freestream density by more than a factor of 20, so the post-shock layer is thin. Figure 2 also shows a pronounced post-shock entropy layer accompanied by strong tangential shear. As the flow turns around the forebody, this shear–entropy layer moves toward the wall and later interacts with the near-wall region.

The response to freestream forcing is best interpreted as a two-stage process. First, the bow shock transmits and amplifies the incoming disturbance. Second, the transmitted disturbance convects within the post-shock domain and undergoes additional growth by extracting energy from the base flow. To quantify these contributions, let  $\dot{E}_{PS}(t)$  denote the surface-integrated disturbance-energy flux evaluated immediately downstream of the shock. We define the net increase of disturbance-energy flux across the shock as

$$\Delta\dot{E}_S(t) = \dot{E}_{PS}(t) - \dot{E}_\infty(t).$$

The cycle-averaged decomposition used below is

$$\overline{G}_S^{\text{opt}} = \frac{\overline{\Delta\dot{E}_S}}{\overline{\dot{E}_\infty}}, \quad \overline{G}_D^{\text{opt}} = \frac{\overline{E}}{\overline{\Delta\dot{E}_S} T^{\text{ref}}}, \quad \overline{G}_T^{\text{opt}} = \frac{\overline{E}}{\overline{\dot{E}_\infty} T^{\text{ref}}} = \overline{G}_S^{\text{opt}} \overline{G}_D^{\text{opt}}.$$

Here  $\overline{E}$  is the cycle-averaged disturbance energy stored in the post-shock domain, and  $T^{\text{ref}}$  is the reference time defined in §II C 1. Thus,  $\overline{G}_S^{\text{opt}}$  measures the net shock-induced increase of disturbance-energy flux relative to the incident flux, whereas  $\overline{G}_D^{\text{opt}}$  measures the storage and convective amplification inside the post-shock domain relative to that net transmitted input.

Table II lists the cycle-averaged gains for the five leading optimal freestream forcing modes. For the leading mode, the shock contributes  $\overline{G}_S^{\text{opt}} = 422$  and the downstream evolution contributes  $\overline{G}_D^{\text{opt}} = 1870$ , yielding a total cycle-averaged gain  $\overline{G}_T^{\text{opt}} = 7.9 \times 10^5$ . The large response is therefore not produced by shock transmission alone: it results from the combination of strong shock amplification and subsequent convective growth within the post-shock layer.

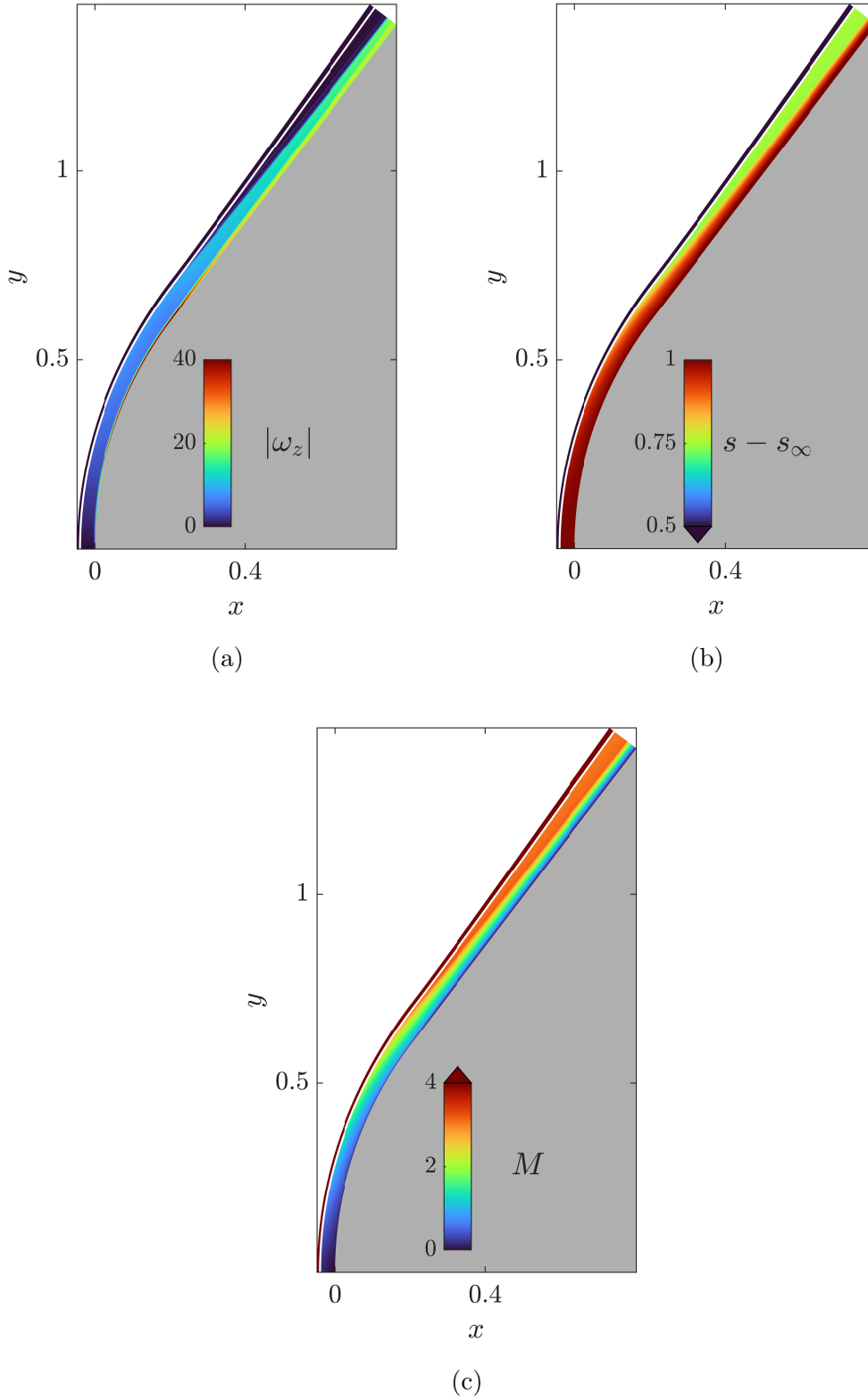


FIG. 2: Steady base flow computed with the freestream conditions from table I at  $Re_\infty = 285\,000$  and  $M_\infty = 28.7$ . The capsule is colored in gray. The bow shock is indicated by a solid white line. (a) Vorticity. (b) Entropy. (c) Mach number. All variables are non-dimensionalized as described in §II B 1, while entropy is non-dimensionalized with the freestream entropy  $s_\infty$ .

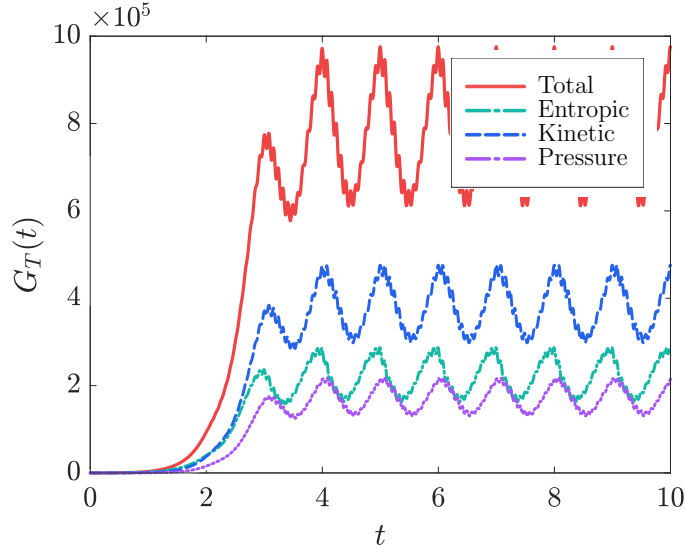


FIG. 3: Instantaneous total gain  $G_T(t)$  for the leading optimal freestream forcing mode. After the initial transient, the response approaches a time-periodic state whose maximum-over-phase gain is  $G_{T,\max}^{\text{opt}} = 9.7 \times 10^5$ . Base flow computed with freestream conditions from table I at  $Re_\infty = 285\,000$  and  $M_\infty = 28.7$ . Time is non-dimensionalized as described in §II B 1.

Figure 3 shows the instantaneous gain  $G_T(t)$  for the leading optimal forcing mode. After an initial transient, the response becomes time-periodic. The maximum gain is  $G_{T,\max}^{\text{opt}} = 9.7 \times 10^5$ , whereas the corresponding cycle-averaged gain is the value reported in table II. In the periodic regime, the post-shock disturbance energy, when partitioned according to the Chu-energy norm (equation 15), is dominated by the kinetic term, which accounts for approximately 50% of the total, while the pressure and entropy terms contribute roughly 25% each.

The Chu-energy partition of the optimal upstream forcing is reported in table III. The five leading optimal modes consist of approximately 73% pressure energy, 26% entropy energy, and less than 2% kinetic energy. This partition is computed from the Chu energy norm of equation 15, evaluated immediately upstream of the bow shock. While the Chu norm is closely related to the Kovásznyai modal decomposition, the two are not equivalent. For the Kovásznyai modes, LIA predicts transmitted disturbance-energy fluxes that scale as  $O(M_1^2)$  in the strong-shock limit, where  $M_1$  denotes the pre-shock Mach number [14]. By contrast, incident vortical Kovásznyai modes exhibit only order-unity kinetic-energy amplification across the shock [15]. Because  $M_1 = M_\infty = 28.7$  in the present case, this shock-transmission scaling favors incident disturbances with acoustic or entropic character over vortical disturbances. Hence, the optimization selects an upstream trace with little vortical-energy content and strong acoustic/entropic content, which is the part of the admissible disturbance space expected from LIA to couple most efficiently through the bow shock.

The spatial structure of the leading mode is shown in figure 4. Since the optimal freestream disturbance is available only immediately upstream of the fitted bow shock, the wave packet shown in figure 4a is reconstructed by projecting the optimal disturbance onto Kovásznyai modes. The reconstruction is nearly exact, with an accuracy close to 100%. Further details are provided in Appendix D. At  $t = 0$  the reconstructed forcing is arranged so that the

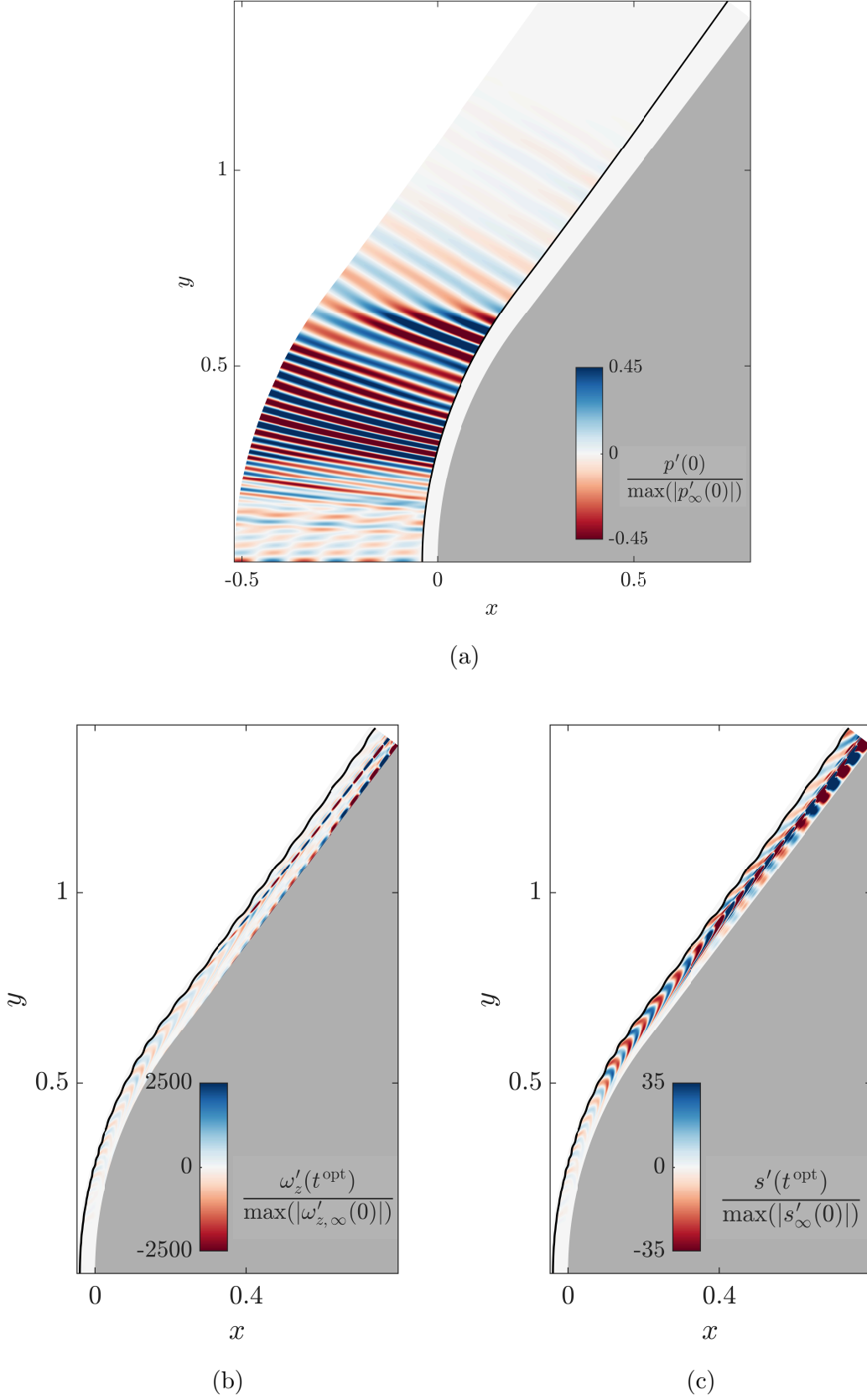


FIG. 4: Leading optimal freestream forcing mode. Base flow computed with freestream conditions from table I. The fitted-shock location is indicated by the black line.  $Re_\infty = 285\,000$  and  $M_\infty = 28.7$ . (a) Pressure at  $t = 0$ . (b) Vorticity at the instant of peak gain on the limit cycle. (c) Entropy at the same instant. All variables are non-dimensionalized as described in §II B 1.

Mode	Pressure (%)	Entropic (%)	Kinetic (%)
1	73.2	25.6	1.2
2	73.3	25.5	1.2
3	73.0	25.7	1.3
4	72.7	25.8	1.5
5	72.7	25.8	1.5

TABLE III: Energy composition immediately upstream of the bow shock for the five leading optimal freestream-forcing modes, expressed in terms of the Chu-energy norm at  $Re_\infty = 285\,000$  and  $M_\infty = 28.7$ .

transmitted packet enters the shear–entropy layer near the region where the shock curvature varies most rapidly (figure 4a). As the packet convects downstream, it develops both vorticity and entropy signatures (figures 4b and 4c) that amplify along the shear–entropy layer. The later interaction with the near-wall region is secondary: it reflects the advection of the layer toward the wall and does not require a separate classical boundary-layer instability.

## B. Energetics of the optimal disturbance

To identify the source of the downstream growth, we examine the kinetic and entropic energy budgets associated with the Chu norm integrated over the post-shock region  $V_D$ . We denote  $\langle f \rangle_D \equiv \int_{V_D} f dV$ , and define the kinetic energy contribution to Chu’s norm as  $E^k = \langle 1/2\rho_0 u'_i u'_i \rangle_D$ . The corresponding kinetic-energy budget is

$$\frac{dE^k}{dt} = \langle \mathcal{A}^k \rangle_D + \langle \mathcal{P}^k \rangle_D + \langle \Pi_d^k \rangle_D + \langle \mathcal{T}^k \rangle_D + \langle \mathcal{D}^k \rangle_D, \quad (27)$$

where  $\mathcal{A}^k$  is advection of perturbation kinetic energy by the base flow,  $\mathcal{P}^k$  is production by base-flow velocity gradients,  $\Pi_d^k$  is pressure–dilatation,  $\mathcal{T}^k$  is the combined pressure and viscous transport, and  $\mathcal{D}^k$  is viscous dissipation. The entropic budget for  $E^s = \langle (\gamma_0^* - 1)p_0 / (2\gamma_0^*) (s' / R_{g,0})^2 \rangle_D$  is

$$\frac{dE^s}{dt} = \langle \mathcal{A}^s \rangle_D + \langle \mathcal{P}^s \rangle_D + \langle \mathcal{T}^s \rangle_D + \langle \mathcal{D}^s \rangle_D + \langle \mathcal{S}^s \rangle_D, \quad (28)$$

where  $\mathcal{A}^s$  is base-flow advection of entropic energy,  $\mathcal{P}^s$  is production by perturbation advection of the base-flow entropy gradient,  $\mathcal{T}^s$  is heat-flux transport,  $\mathcal{D}^s$  is diffusive dissipation, and  $\mathcal{S}^s$  is the source associated with viscous heating. For compactness, the brackets  $\langle \cdot \rangle_D$  are omitted below when referring to domain-integrated budget terms. The detailed derivation of these budgets is given in Appendix B.

Figure 5 shows that, once the disturbance is inside the post-shock domain, the dominant positive term is the production  $\mathcal{P}^k$ . In the domain-integrated budget, this production is balanced primarily by advective removal  $\mathcal{A}^k$  and transport  $\mathcal{T}^k$ . Viscous dissipation is negligible at this Reynolds number, and pressure dilatation makes only a minor contribution to the

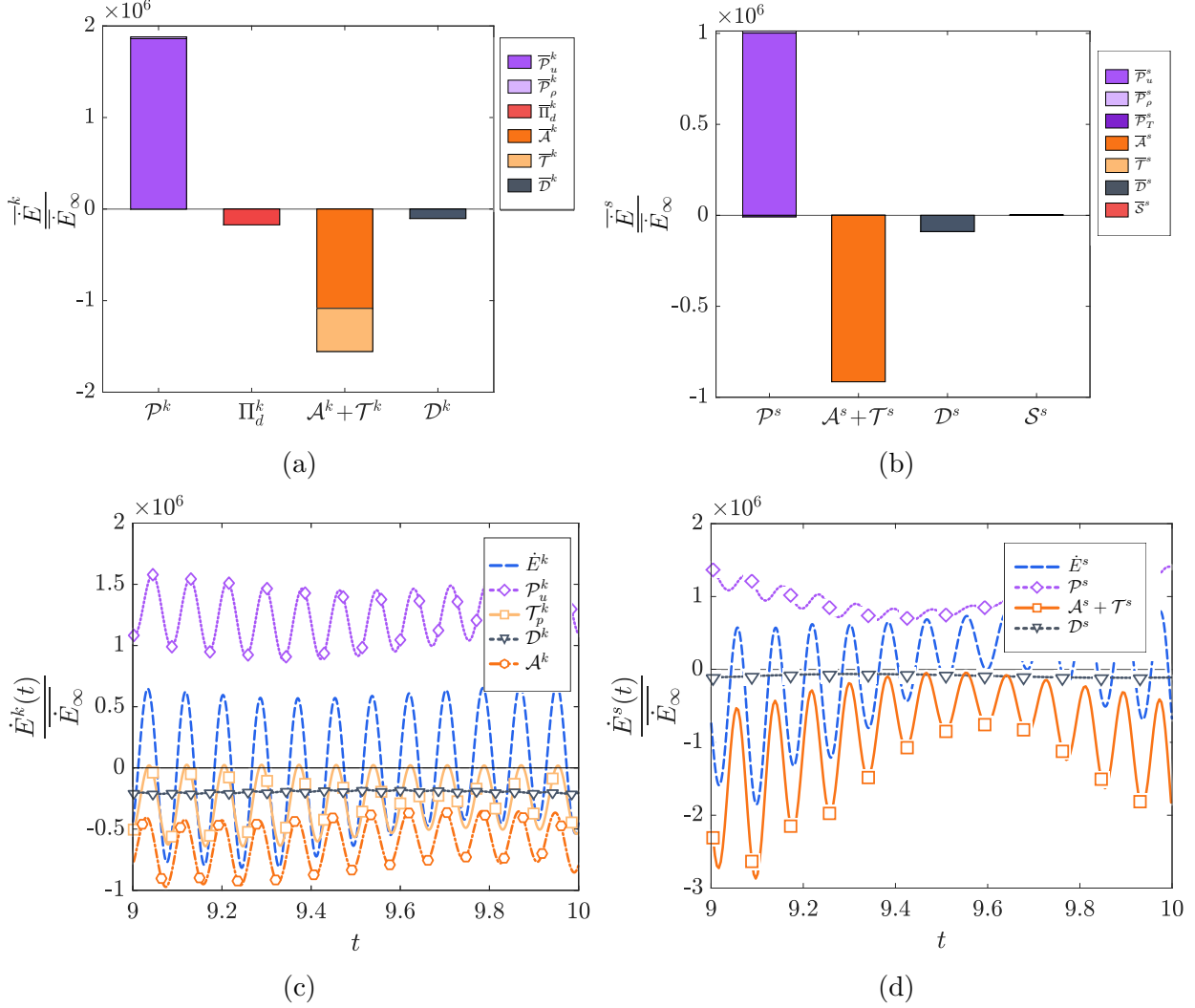


FIG. 5: Post-shock domain-integrated kinetic and entropic Chu-energy budgets for the leading optimal freestream forcing mode. The base flow is computed using freestream conditions from table I at  $Re_\infty = 285\,000$  and  $M_\infty = 28.7$ . Energy rates are normalized by the cycle-averaged freestream disturbance-energy flux crossing the shock,  $\overline{E}_\infty$ . Budget term definitions appear in Appendix B. (a) Spatially and time-averaged mean kinetic energy budget over one period. (b) Entropy budget corresponding to panel (a). (c) Spatially averaged kinetic budget terms as functions of time over one period. (d) Corresponding entropy budget terms as in panel (c).

kinetic-energy balance.

The dominant local source of kinetic energy is the Reynolds-stress production term,

$$\mathcal{P}_u^k = -\rho_0 u'_i u'_j \frac{\partial u_{i,0}}{\partial x_j}.$$

Positive  $\mathcal{P}_u^k$  therefore corresponds to extraction of mean kinetic energy by the fluctuations. The spatial distribution of this term, shown in figure 6a, is concentrated in the post-shock shear-entropy layer and intensifies as the packets convect downstream. Near the wall, the

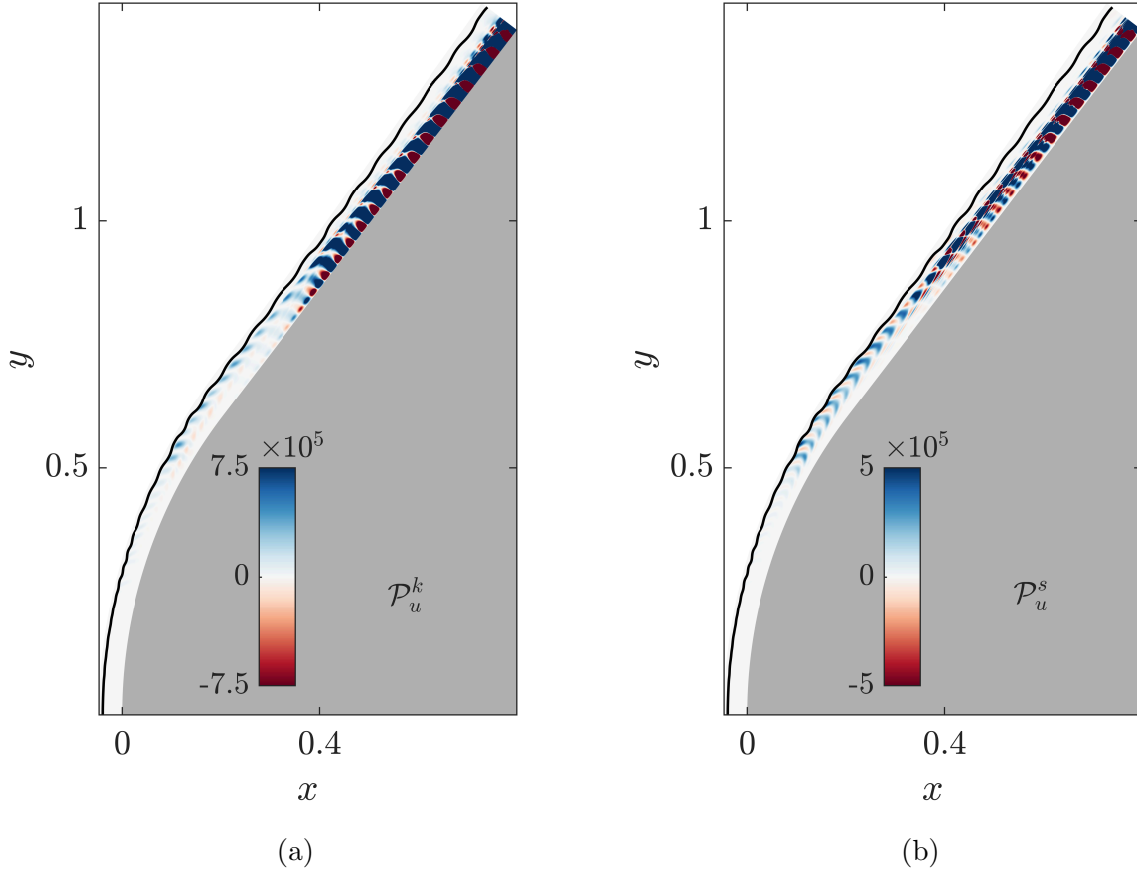


FIG. 6: Contours of the dominant production terms in the kinetic and entropic budgets for the leading optimal freestream forcing mode, shown at the instant of maximum gain during one period. The base flow is computed using freestream conditions from table I with  $Re_\infty = 285\,000$  and  $M_\infty = 28.7$ . Both  $\mathcal{P}_u^k$  and  $\mathcal{P}_u^s$  are normalized by  $\overline{E}_\infty/V_D$ . (a) Reynolds-stress production term in the kinetic budget:  $\mathcal{P}_u^k$ . (b) Entropic production term due to velocity fluctuations:  $\mathcal{P}_u^s$ .

term exhibits both signs because the no-slip condition restricts the fluctuation field, but the strongest positive contribution remains outside the boundary layer, in the outer part of the post-shock layer.

The first dominant negative contribution in the domain-integrated kinetic-energy budget is the advective flux,

$$\mathcal{A}^k = -\rho_0 u_{j,0} \frac{\partial}{\partial x_j} \left( \frac{1}{2} u'_i u'_i \right),$$

whose negative peaks occur whenever a disturbance packet leaves the computational domain. Under continuous freestream forcing, the long-time response is periodic, so successive packets produce a sequence of such peaks. The second dominant negative contribution is the pressure-transport term,

$$\mathcal{T}_p^k = \frac{\partial}{\partial x_j} (-u'_j p').$$

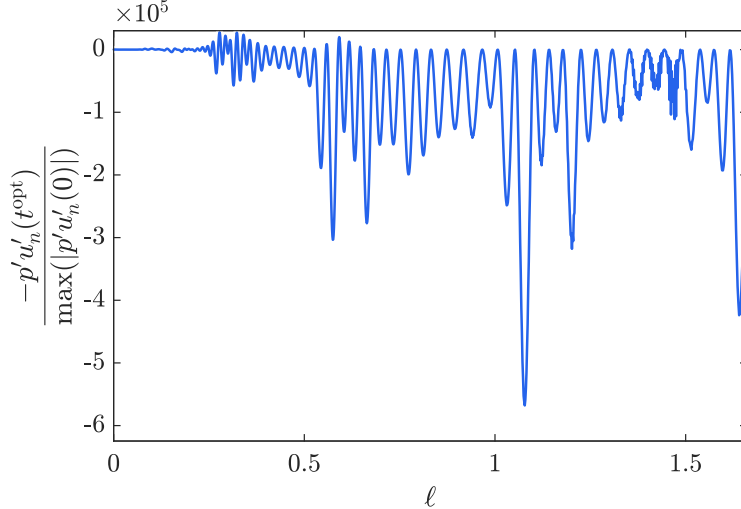


FIG. 7: Shock integrand of the pressure-work term,  $-p'u'_n$ , evaluated immediately downstream of the bow shock, where  $u'_n$  is the disturbance velocity component normal to the shock. The horizontal axis is the nondimensional arc length  $l/R$  measured along the shock from the axis of symmetry. The result is for the leading optimal freestream forcing mode at the instant of peak gain on the limit cycle  $t^{\text{opt}}$ . Base flow computed with freestream conditions from table I at  $Re_\infty = 285\,000$  and  $M_\infty = 28.7$ .

Because  $\mathcal{T}_p^k$  is a divergence term, its domain integral reduces to a boundary flux. The wall and the symmetry axis do not contribute because  $u'_n = 0$  there; thus, the dominant contribution arises at the bow shock, with a smaller contribution at the outflow. Figure 7 shows the shock integrand,  $-u'_n p'$ , immediately downstream of the shock. With the outward normal convention used in the domain integral, its predominantly negative sign indicates that pressure transport removes kinetic energy from the post-shock perturbation field through the fitted-shock boundary. Conversely, the disturbance field performs a substantial amount of work on the bow shock, causing it to become corrugated. As discussed later, this introduces a strong feedback mechanism. This effect is present because shock displacement is retained in the linearization of the bow shock. In the fixed-shock approximation adopted in the preliminary study of Antón-Álvarez and Lozano-Durán [30], this mechanism is suppressed.

The entropic budget has the same overall structure: production dominates and is balanced mainly by advection. Its leading source term is

$$\mathcal{P}_u^s = -\frac{(\gamma_0^* - 1)p_0}{\gamma_0^* R_{g,0}^2} u'_j s'_j \frac{\partial s_0}{\partial x_j}.$$

This term shows that entropic amplification is driven by advection of the base-flow entropy gradient by the velocity fluctuations amplified in the shear-entropy layer. Figure 6b confirms that  $\mathcal{P}_u^s$  is collocated with  $\mathcal{P}_u^k$ : wherever the shear layer amplifies velocity fluctuations, the same fluctuations also amplify the entropic component. A key difference from the kinetic budget is that the entropic budget has no comparably strong shock-pressure-work sink. The transport term  $\mathcal{T}^s$  and diffusive dissipation are both small, so entropic energy continues to increase until the packet is advected out of the domain.

$Re_\infty$	$\overline{G}_S^{\text{opt}}$	$\overline{G}_D^{\text{opt}}$	$\overline{G}_T^{\text{opt}}$
10 000	452	9.64	4 360
20 000	450	33.1	14 900
50 000	439	362	159 000
100 000	428	1189	509 000
200 000	422	1635	690 000
285 000	422	1870	790 000
500 000	421	2143	902 000

TABLE IV: Cycle-averaged optimal gain across the shock and within the post-shock flow at different Reynolds numbers. The values are computed after the response has reached its asymptotic periodic state. The reported gains correspond to the optimal freestream disturbance that maximizes  $G_T^{\text{opt}}$  at  $M_\infty = 28.7$ .

The resulting picture is as follows: shock transmission produces an optimal freestream disturbance dominated by acoustic and entropy components of the Chu energy partition, and the post-shock shear-entropy layer amplifies this response convectively. The disturbances then impinge back on the bow shock, generating shock corrugation. For the present optimal response, a separate classical boundary-layer mode is not needed to account for the dominant computed gain.

### C. Scaling analysis of the gain

We investigate the scaling laws governing the gain as a function of  $Re_\infty$ ,  $M_\infty$ , and  $\gamma_2^*$ . The analysis is divided into two steps: the scaling of the shock-transmission gain and that of the post-shock convective gain. We also investigate the nonlinear feedback between post-shock disturbances and bow shock corrugation.

#### 1. Shock-transmission gain

We first examine the dependence of the cycle-averaged, shock-transmission gain  $\overline{G}_S^{\text{opt}}$  on  $Re_\infty$  at fixed  $M_\infty = 28.7$ . The results are reported in table IV. The shock gain is nearly independent of Reynolds number, with  $\overline{G}_S^{\text{opt}} \approx 4 \times 10^2$  throughout the range considered. This weak dependence is expected because the leading amplification across the bow shock is governed by the linearized Rankine–Hugoniot jump conditions, which are inviscid. At fixed upstream thermochemical state and capsule geometry, Reynolds-number effects can therefore enter  $\overline{G}_S^{\text{opt}}$  only through small viscous changes to the base flow and shock shape.

The Mach-number scaling of  $\overline{G}_S^{\text{opt}}$  is explained by classical LIA theory [14], in which the ratio of post-shock disturbance energy flux,  $\Delta \dot{E}_S$ , to the freestream disturbance energy flux,  $\dot{E}_\infty$ , scales as  $\Delta \dot{E}_S / \dot{E}_\infty = \mathcal{O}(M_1^2)$  for high Mach numbers. One correction added relative to the classical theory is the inclusion of the effective  $\gamma_2^*$ , yielding the scaling  $\overline{G}_S^{\text{opt}} \sim \gamma_2^* M_1^2$ . Figure 8a presents the energy amplification across the shock for the optimal disturbances at

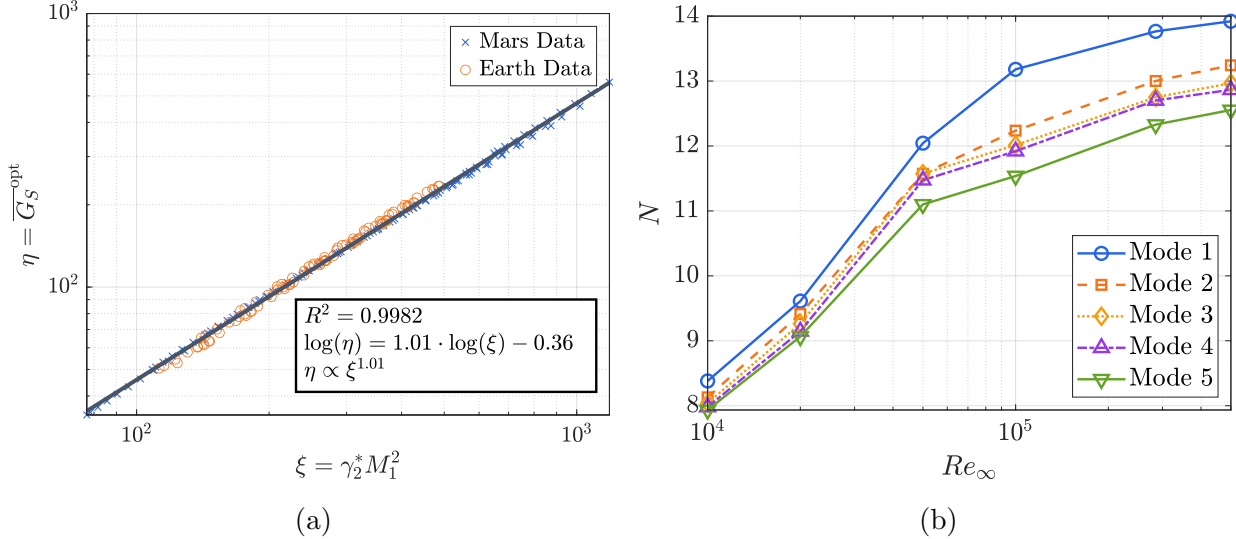


FIG. 8: Energy gains of the optimal disturbance. (a) Optimal gain across the shock,  $\overline{G}_S^{\text{opt}}$ , expressed in terms of the scaling parameters, with a linear fit overlaid. Freestream conditions are varied to probe the scaling of the shock gain. (b) Energy-gain logarithm,  $N = \ln G_{T,\text{max}}^{\text{opt}}$ , as a function of  $Re_\infty$  with the remaining freestream conditions fixed to those of table I.

different flight conditions, compared with the theoretical scaling  $\gamma_2^* M_1^2$ . The collapse of both the Mars and Earth data onto this predicted scaling supports the dominant role of Mach number in the shock-induced amplification of acoustic and entropic disturbances.

## 2. Post-shock convective gain

The post-shock gain scaling is computed for a fixed capsule geometry (see §II A). As reported in table IV, the downstream gain increases monotonically with  $Re_\infty$ , at a rate that decreases with increasing Reynolds number. This behavior is made explicit in figure 8b, which shows the energy-gain logarithm of the maximum steady-state gain, defined as  $N = \ln G_{T,\text{max}}^{\text{opt}}$ . The progressive weakening of the  $Re_\infty$  dependence suggests that the downstream amplification approaches a high-Reynolds-number, convectively-dominated limit, in which finite- $Re_\infty$  effects enter only as a viscous and thermal diffusive correction to an otherwise inviscid growth process.

To study this observation, we construct a scaling argument for the downstream gain that isolates the inviscid and viscous contributions. The point of departure is the energy-budget analysis of §III B, which establishes two facts that are central to what follows. First, the kinetic part of the Chu energy is the largest single contribution to the optimal response. Second, within the kinetic-energy budget the leading production mechanism is Reynolds-stress work against the mean shear of the shock-induced shear-entropy layer. Guided by these observations, we write a local Chu-energy balance for a convecting wave packet in which inviscid shear production is balanced by viscous dissipation,

$$\frac{1}{E} \frac{DE}{Dt} \sim \chi \frac{\partial U_t}{\partial y_n} - \frac{k_{\text{eff}}^2}{Re_\infty}, \quad (29)$$

where  $E$  denotes a local Chu-energy density along the wave-packet trajectory,  $y_n$  is a cross-layer coordinate, and  $U_t$  is the tangential base-flow velocity. The coefficient  $\chi = O(1)$  represents the correlation between the velocity fluctuations and the mean shear, and  $k_{\text{eff}}$  is the characteristic wavenumber of the downstream packet. The first term in (29) represents kinetic production due to Reynolds stresses ( $\mathcal{P}_u^k$ ), whereas the second term represents viscous damping ( $\mathcal{D}^k$ ).

The production term is controlled by the shear across the shear–entropy layer  $\partial U_t / \partial y_n \sim \Delta U_t / \delta_s$ , where  $\delta_s$  is its characteristic thickness. For the fixed capsule geometry and the family of freestream states considered here, variations of  $\Delta U_t$  are weaker than the changes associated with the layer thickness and are absorbed into the fitted constant below. In the hypersonic blunt-body limit, the thickness of the shock-generated shear–entropy layer is taken to scale with the shock standoff distance  $d$ . We therefore use  $\delta_s / R \sim d / R \sim (\rho_2 / \rho_1)^{-1}$ , where  $\rho_1$  and  $\rho_2$  are the pre- and post-shock densities of the corresponding normal-shock state. Thus larger compression produces a thinner shock layer and a steeper shear–entropy layer. Integrating the production part of (29) over the residence time of the packet therefore gives

$$\int \chi \frac{\partial U_t}{\partial y_n} dt \sim \frac{\rho_2 / \rho_1}{C}, \quad (30)$$

where  $C$  is a positive constant containing the geometric factors including shock obliquity and curvature, the residence length, the convective speed, the proportionality between  $\delta_s$  and  $d$ , and the production-efficiency factor  $\chi$ .

The Reynolds-number correction follows from the dissipative term in (29). We model the characteristic wavenumber selected by the optimal packet as  $k_{\text{eff}} \sim Re_\infty^{1/4}$ , where the exponent 1/4 is chosen so that the viscous correction follows the Reynolds-number dependence observed in the computed optimal gains. This scaling suggests that the global input–output problem selects an intermediate disturbance scale, and is reminiscent of mixed viscous–inviscid scale selections that arise in other stability and receptivity analyses [31, 32].

Combining (30) and the viscous correction from (29), the downstream amplification factorizes into an inviscid and a viscous contribution,

$$\overline{G}_D^{\text{opt}} \sim \overline{G}_{D,I}^{\text{opt}} \overline{G}_{D,V}^{\text{opt}} \sim \exp\left[\frac{\rho_2 / \rho_1}{C}\right] \exp\left[-\frac{B}{\sqrt{Re_\infty}}\right], \quad (31)$$

where  $C$  and  $B$  are treated as constants for a fixed body geometry and a fixed class of optimal disturbance paths. The first exponential represents the inviscid convective production within the compressed shear–entropy layer; the second encodes the leading viscous correction. Equation (31) is tested in two complementary sweeps designed to isolate each factor. We first fix the freestream conditions of table I and vary  $Re_\infty$  to determine  $B$  within  $\overline{G}_{D,V}^{\text{opt}}$ . The results are shown in figure 9a. We next fix  $Re_\infty = 285\,000$  and vary the freestream Mach number and the atmospheric composition (Earth and Mars), so that only the inviscid factor  $\overline{G}_{D,I}^{\text{opt}}$  is isolated. The resulting collapse, shown in figure 9b, is reasonable given the simplifying assumptions underlying (30), and supports the interpretation of  $\rho_2 / \rho_1$  as the controlling inviscid parameter.

The compression ratio itself carries a non-trivial Mach-number dependence that is worth

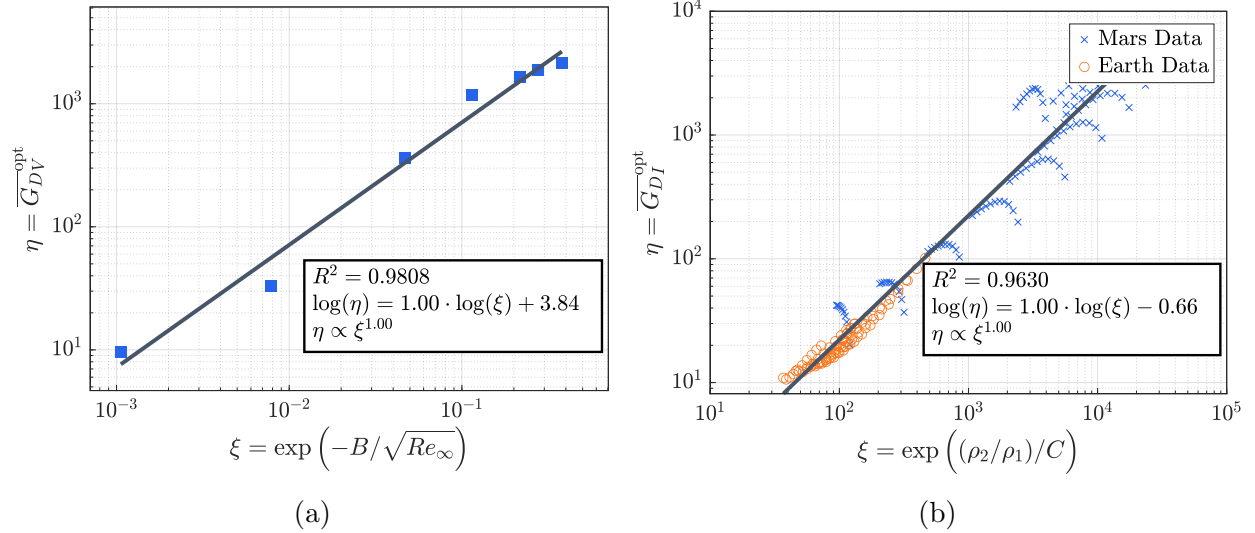


FIG. 9: Determination of the viscous,  $\overline{G}_{D,V}^{\text{opt}}$ , and inviscid,  $\overline{G}_{D,I}^{\text{opt}}$ , contributions to the downstream optimal gain  $\overline{G}_D^{\text{opt}}$ . Energy gains are plotted against the corresponding scaling parameters. Mars and Earth data are both obtained from the present stability-analysis computations; linear fits are superimposed. (a) Viscous scaling  $\overline{G}_{D,V}^{\text{opt}}$ : freestream conditions are fixed to those of table I, and  $Re_\infty$  is varied; the best-fit constant is  $B = 685$ . (b) Inviscid scaling  $\overline{G}_{D,I}^{\text{opt}}$ : the Reynolds number is fixed at  $Re_\infty = 285\,000$ , while the freestream Mach number and atmospheric composition (Earth and Mars) are varied; the best-fit constant is  $C = 2.23$ .

making explicit. For a calorically perfect gas, the Rankine–Hugoniot relations give

$$\frac{\rho_2}{\rho_1} = \frac{(\gamma + 1)M_{n,1}^2}{(\gamma - 1)M_{n,1}^2 + 2}, \quad (32)$$

with  $M_{n,1}$  the shock-normal Mach number, so that  $\rho_2/\rho_1$  and hence  $\overline{G}_{D,I}^{\text{opt}}$  saturate at a finite high-Mach-number limit. In the high-enthalpy regime relevant to planetary entry, however, vibrational excitation and dissociation reduce the effective post-shock specific-heat ratio and allow for substantially larger compression ratios. The downstream gain can therefore continue to grow with  $M_\infty$  through the thermochemical dependence of  $\rho_2/\rho_1$  on the post-shock state. This mechanism provides a direct route by which imperfect-gas effects enhance the downstream amplification beyond the perfect-gas bound.

Finally, combining the two stages of the amplification process yields a total scaling factor of

$$\overline{G}_T^{\text{opt}} \sim \gamma_2^* M_1^2 \exp \left[ \frac{\rho_2/\rho_1}{C} - \frac{B}{\sqrt{Re_\infty}} \right]. \quad (33)$$

Figure 10 presents the cycle-averaged total gain  $\overline{G}_T^{\text{opt}}$  obtained with the optimal freestream disturbances, plotted against the right-hand side of (33). The constants fitted from the present numerical experiments are  $C = 2.23$  and  $B = 685$ . Despite the simplifying assumptions used in the derivation, the data collapse is reasonable. This agreement supports the interpretation that shock transmission and shear-driven production are the dominant

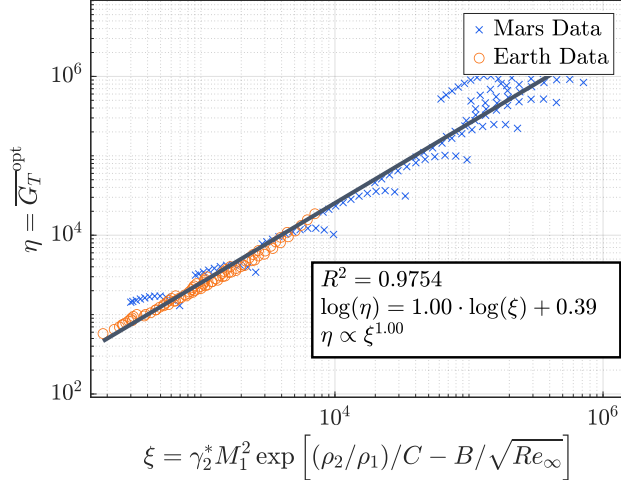


FIG. 10: Total cycle-averaged optimal gain  $\overline{G}_T^{\text{opt}}$  expressed in terms of the scaling parameter in (33). Both Mars and Earth data are obtained from the present receptivity-analysis computations. A linear fit is superimposed. The fitted constants are  $C = 2.23$  and  $B = 685$ .

amplification mechanisms in this regime.

#### D. Feedback via shock corrugation

The gains discussed above quantify the open-loop, linear amplification of a prescribed freestream disturbance. By construction, this approach cannot account for the finite-amplitude feedback through which the amplified downstream disturbance modifies the shock profile itself. In this section, we show that the feedback loop:

shear–entropy layer  $\rightarrow$  bow-shock corrugation  $\rightarrow$  shear–entropy layer,

reinforces the instability over short times.

The feedback mechanism can be understood in terms of the vorticity deposited by the curved bow shock. For a uniform upstream flow, the magnitude of the out-of-plane vorticity generated immediately behind a curved shock has the strong-shock scaling [33]

$$\frac{|\omega_{2,z}|R}{U_\infty} \simeq |\cos \beta| |\kappa|R \left(1 - \frac{\rho_1}{\rho_2}\right)^2 \frac{\rho_2}{\rho_1}, \quad (34)$$

where  $z$  is the direction normal to the meridional plane,  $\kappa$  is the local shock curvature, and  $\beta$  is the angle between the local shock tangent and the freestream direction, so that  $\beta = \pi/2$  for a locally normal shock. This deposited vorticity is then advected downstream and forms the post-shock shear–entropy layer in which the dominant Reynolds-stress production term,  $\mathcal{P}_u^k \sim \partial U_t / \partial y_n \sim |\omega_{2,z}|$ , amplifies the disturbance energy that contributes to  $G_D$ . This estimate is consistent with the baseline scaling from the previous section, where the same shear was approximated as  $\Delta U_t / \delta_s$ . Here,  $|\omega_{2,z}|$  is used to retain the additional dependence on shock corrugation.

At that point, the feedback process can be decomposed into three stages:

- Perturbations transmitted through the bow shock enter the shear–entropy layer and are amplified as they convect downstream. Their pressure component,  $p'$ , impinges on the bow shock and produces a finite corrugation. The level of corrugation is especially high for bow shocks with a small standoff distance, as is typical of the large post-shock compression ratios encountered under the high-enthalpy Martian-entry conditions considered here.
- The corrugated shock modifies the local shock-jump conditions. Because the vorticity deposited by a curved shock depends on both the local curvature and the local shock angle, even a modest corrugation changes the vorticity injected into the post-shock region. The additional vorticity advects downstream and reinforces the shear–entropy layer, strengthening the downstream amplification of disturbances.
- The amplified shear–entropy-layer fluctuations generate a larger pressure imprint on the shock, which increases the shock corrugation even more and the loop closes. From the scaling analysis of  $G_D$  above, for which  $\partial U_t/\partial y_n \sim |\omega_{2,z}|$ , and assuming that the vorticity is simply advected and conserved along streamlines, we expect

$$\Delta N = \ln \left( \frac{G_D^{\text{feedback}}}{G_D} \right) = \mathcal{O} \left( \frac{|\omega_{2,z}|^{\text{corrugated}}}{|\omega_{2,z}|} - 1 \right),$$

where  $G_D^{\text{feedback}}$  is the feedback-modified gain after one advection time of the disturbances.

To assess the strength of the feedback, we perturb the bow shock using the optimal shock-displacement shape obtained in Section III A, scaled to a finite amplitude  $\epsilon$ , and recompute the post-shock azimuthal vorticity injection for the resulting corrugated-shock geometry, denoted by  $J_\omega(\epsilon) = \int_S \rho_2 u_{2,n} |\omega_{2,z}| dA$ . Figure 11 shows the variation in the flux of absolute vorticity across the shock as a function of  $\epsilon$ . If  $J_\omega$  is taken as an integral proxy for the vorticity supplied to the shear layer, such that  $|\omega_{2,z}(\epsilon)|/|\omega_{2,z}(0)| \sim J_\omega(\epsilon)/J_\omega(0)$ , the results indicate that, even for corrugation amplitudes as small as 1% of the capsule radius, the vorticity content of the mean shear increases by a factor of 50. This corresponds to  $\Delta N = \ln(G_D^{\text{feedback}}/G_D) \approx \mathcal{O}(10)$ , whose large magnitude suggests a strong coupling induced by bow-shock corrugation.

The implications are twofold. First, the linear gains reported in Section III A should be regarded as open-loop gains: once the disturbance reaches an amplitude at which the induced shock corrugation is no longer negligible, the production term  $\mathcal{P}_u^k$  in the kinetic budget acquires an additional self-sustaining contribution that is absent from the linearized operator. Second, the feedback loop provides a plausible route to a secondary instability and to an accelerated transition scenario through the breakdown of the bow shock itself, before transition occurs in either the boundary layer or the shear–entropy layer.

### E. Velocity–altitude energy-gain maps for EDL vehicles

We next map the energy-gain logarithm  $N$  over velocity–altitude space for Mars and Earth entry conditions. Motivated by the scaling in (33), we assume that the Reynolds numbers

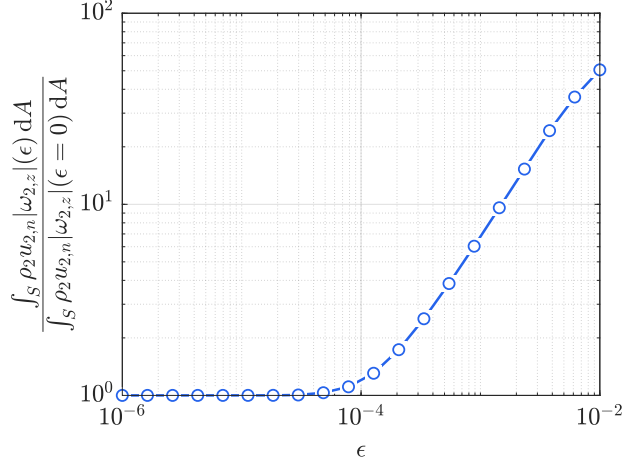


FIG. 11: Increase in the absolute vorticity flux across the bow shock induced by finite-amplitude shock corrugation. The plotted ratio compares the vorticity injection of the baseline shock, computed with the freestream conditions from table I, with that obtained after imposing a finite shock disturbance of amplitude  $\epsilon$ . The imposed shock disturbance has the shape of the corrugation induced by the leading optimal freestream mode in §III A.

in this range are large enough that variations in  $Re_\infty$  produce only secondary corrections to  $N$ . Accordingly, all computations in this map are performed at  $Re_\infty = 285\,000$ . The velocity–altitude sweeps assume chemical and thermal equilibrium. Nonequilibrium effects are expected where the chemical or vibrational relaxation times become comparable to the shock-layer residence time; however, as discussed in Appendix A, the largest amplification factors occur in the region where the equilibrium approximation is justified.

Figure 12 presents  $N$  over velocity–altitude space for both Earth and Mars atmospheres. For reference, the figure also depicts the entry trajectories of the MSL (Mars entry) and Apollo 11 (Earth entry) capsules. The energy-gain logarithms for re-entry in the Earth atmosphere (figure 12a) are clearly smaller than those for the Mars atmosphere (figure 12b). The reduced disturbance amplification in Earth’s atmosphere, relative to Mars, can be attributed to two factors. First, the density ratio across the shock is smaller in Earth’s atmosphere because diatomic nitrogen and oxygen store less vibrational energy than the triatomic carbon dioxide that dominates the Martian atmosphere, resulting in lower compression ratios. Second, for the atmospheric states considered here, the lower molecular weight of Earth’s atmosphere and its thermodynamic state give larger sound speeds than in the corresponding Martian cases, leading to lower Mach numbers at comparable entry velocities. These combined effects result in significantly smaller values of the scaling parameter from (33) for Earth entry conditions.

The results for the Martian atmosphere also reveal a pronounced, localized region of peak amplification at high velocities and altitudes. Remarkably, the MSL entry trajectory passes directly through this critical region. The transition location inferred from the MSL flight aeroheating reconstruction [1], which occurred on the leeside at approximately 64s after atmospheric interface, coincides with the region of maximum amplification. A similar observation applies to the Mars 2020/Perseverance mission, which used a geometrically similar aeroshell and followed a comparable entry profile. The reconstructed MEDLI2 aeroheating

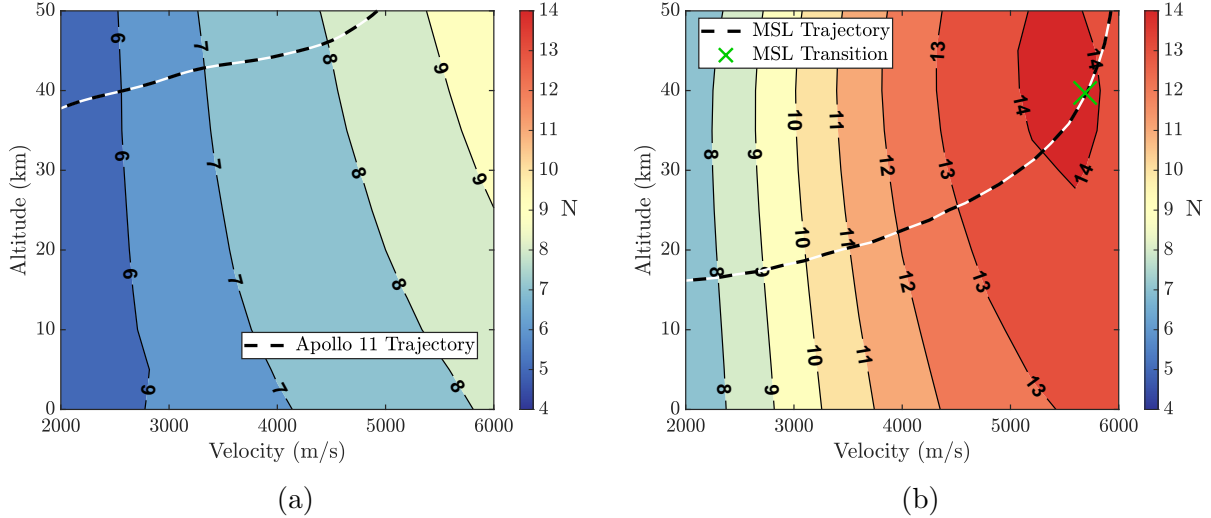


FIG. 12: Energy-gain logarithm  $N = \ln G_{T,\max}^{\text{opt}}$  over a range of velocities and altitudes. The Reynolds number is fixed at  $Re_\infty = 285\,000$ , and all computations assume chemical and thermal equilibrium. For reference, the figure also shows the entry trajectories of the MSL (Mars entry, Edquist *et al.* [10]) and Apollo 11 (Earth entry, Manders [34]) capsules. The transition point inferred from the MSL flight reconstruction [1] is also indicated by a green cross. (a) Earth atmosphere. (b) Mars atmosphere.

data indicate transition-associated heat-flux augmentation in the same region of velocity–altitude space characterized here by elevated amplification factors [2, 6].

### F. Nonlinear WMLES of the MSL configuration

To test whether the amplification mechanism identified by the linear receptivity analysis can proceed to nonlinear breakdown, wall-modeled large-eddy simulations (WMLES) were performed for the MSL entry vehicle under a representative Mars-entry condition. The purpose of the WMLES is not to replace the receptivity analysis, but to determine whether a three-dimensional nonlinear flow develops the same shock/shear–entropy-layer instability and the same qualitative heating footprint. The capsule geometry was taken from Edquist *et al.* [10], and the vehicle was simulated at an angle of attack  $\alpha = 17.3^\circ$ , characteristic of the flight attitude near the transition event. This angle is also consistent with the effective angle of attack used in the receptivity analysis. The freestream state is that of table I, which corresponds to the region of the MSL trajectory in which the reconstructed aerothermal data indicate a strong increase in leeside heating [1]. Similar leeside heating augmentation was also inferred for the geometrically related Mars 2020/Perseverance entry capsule [2, 6].

The simulations were carried out with the charLES solver using a second-order finite-volume discretization with entropy-preserving properties. The unresolved turbulent stresses were modeled with the Vreman subgrid-scale model [35], coupled to an equilibrium, algebraic wall model [36]. The wall was modeled as isothermal, with  $T_w = 700\text{ K}$ , representative of reconstructed heat-shield temperatures near the transition region during MSL entry [1]. The

nondimensional transport coefficients were prescribed by the power laws  $\mu^* = (T/T_\infty)^{3/4}$  and  $k^* = (T/T_\infty)^{3/4}$ .

The gas was modeled as a calorically perfect ideal gas with a prescribed constant effective specific-heat ratio  $\gamma^*$ . This closure is a simplification with respect to the receptivity analysis, as a constant  $\gamma^*$  cannot reproduce the spatially varying composition and temperature-dependent thermodynamics of an equilibrium Mars-entry shock layer. Instead,  $\gamma^*$  is used below as a controlled parameter that changes the post-shock compressibility and density ratio. The rationale for varying  $\gamma^*$  follows from the gain scaling derived in §III C. At fixed geometry and Reynolds number, the leading inviscid part of the freestream-to-shock-layer amplification scales as  $\gamma_2^* M_1^2 \exp[(\rho_2/\rho_1)/C]$ , up to the viscous correction in (33). For a calorically perfect gas, the normal-shock density ratio from (32) shows that  $\rho_2/\rho_1 \rightarrow (\gamma^* + 1)/(\gamma^* - 1)$  in the strong-shock limit  $M_{n,1} \gg 1$  [37]. Thus, lowering  $\gamma^*$  increases the post-shock compression ratio and, through the exponential factor in the gain scaling, increases the downstream convective amplification. In the strong-shock approximation, the corresponding inviscid control parameter is

$$II(\gamma^*) \equiv \gamma^* M_1^2 \exp \left[ \frac{1}{C} \frac{\gamma^* + 1}{\gamma^* - 1} \right].$$

Using the value  $C = 2.23$  obtained in §III C, decreasing  $\gamma^*$  from 1.25 to 1.20 increases  $II$  by a factor of approximately 2.3 at fixed  $M_1$ . The two constant- $\gamma^*$  cases therefore provide a controlled nonlinear test of the same compression- and curvature-driven amplification mechanism identified by the linear analysis. For reference, the equilibrium-gas computations discussed in the receptivity analysis yield spatially varying post-shock values of  $\gamma^*$ , with values as low as approximately 1.08 for Mars-entry conditions and 1.17 for Earth-entry conditions over the range considered here.

The sensitivity of the nonlinear flow to  $\gamma^*$  is shown in figure 13. For  $\gamma^* = 1.25$ , the heat-flux field contains weak streaky modulations near the downstream portion of the leeside, but no large localized heat-flux spike develops. By contrast, the  $\gamma^* = 1.20$  case exhibits a strong, localized increase in leeside heat flux, visible in both the instantaneous and time-averaged fields. No deterministic freestream disturbance was prescribed in these simulations. The initial disturbance amplitude is supplied by the small numerical, grid-scale, and round-off perturbations present in the computation. Consequently, the WMLES should be interpreted as evidence that the flow is nonlinearly susceptible to this instability route, rather than as a calibrated prediction of a transition threshold for a specified freestream disturbance environment.

The region of strongest computed heating lies on the leeside shoulder, consistent with the surface region where post-flight MSL reconstructions inferred the largest transition-associated heating augmentation [1]. The comparison with flight data should nevertheless be interpreted qualitatively rather than as a direct reconstruction of the measured heat-flux histories. The constant- $\gamma^*$  perfect-gas model, the simplified transport closure, the wall model, and the omission of ablation, pyrolysis, radiation, and finite-rate thermochemistry preclude a one-to-one comparison of the absolute heat-flux magnitude. The relevant observation concerns the underlying mechanism: when the compression-controlled amplification is increased, the WMLES produces a localized nonlinear breakdown on the leeside and a corresponding localized heating footprint, consistent with the leeside transition inferred from MSL and Mars 2020/Perseverance flight data [1, 2, 6].

The instantaneous WMLES fields in figure 14 clarify the mechanism producing the elevated

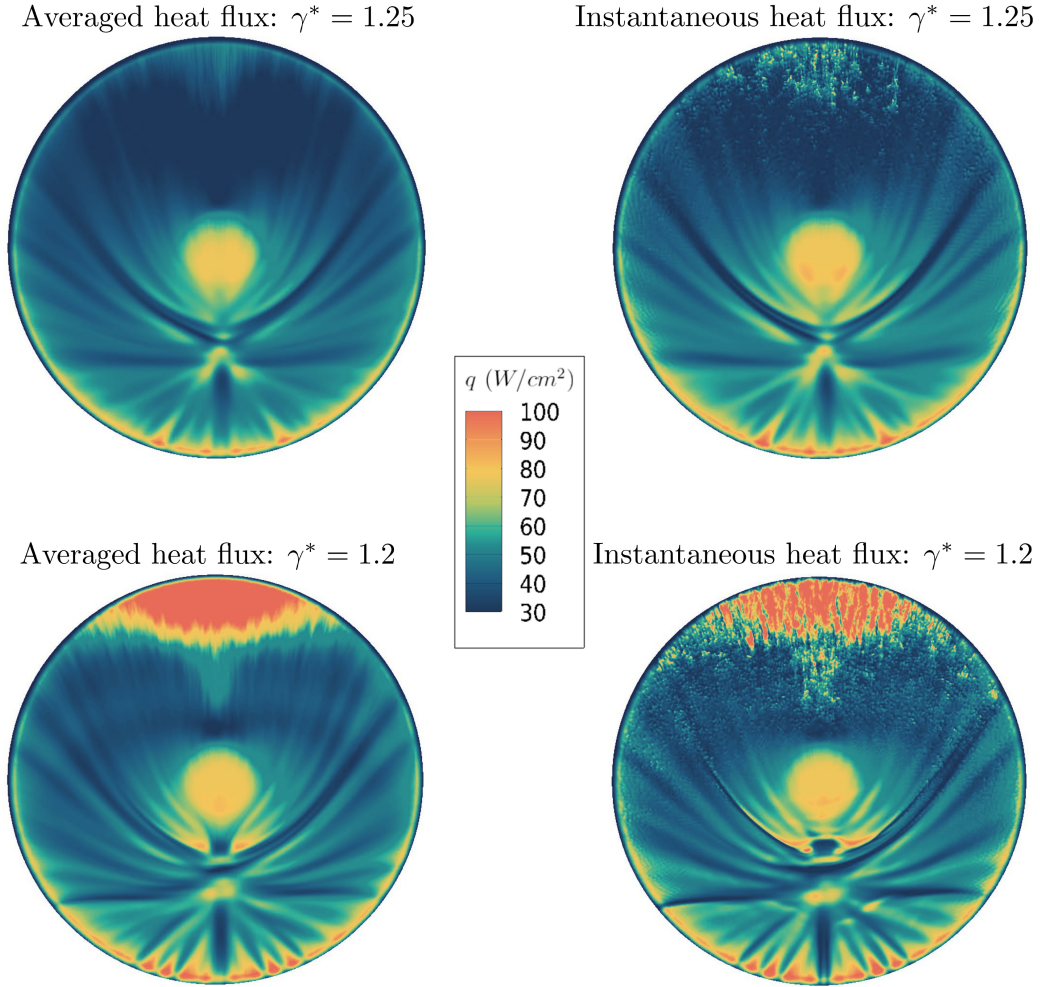


FIG. 13: Time-averaged and instantaneous wall heat flux on the MSL heat shield obtained from WMLES for two values of the constant effective specific-heat ratio  $\gamma^*$ . Freestream conditions from table I for a calorically perfect ideal gas at  $\alpha = 17.3^\circ$ . The leeside corresponds to the upper half of the capsule surface.

leeside heat flux. The velocity magnitude (figure 14a) and out-of-plane vorticity component (figure 14b) show coherent disturbances forming in the shear–entropy layer immediately behind the curved bow shock. These disturbances amplify as they convect downstream, roll up, and eventually break down. The resulting turbulent mixing increases wall-normal transport of high-enthalpy fluid toward the heat shield, producing the localized heat-flux rise. Thus the dominant nonlinear route is the breakdown of the shock-generated shear–entropy layer, rather than the independent onset of a classical boundary-layer instability at the wall.

The same mechanism also explains why the strongest transition signature is localized on the leeside. In both the WMLES and the flight reconstructions, no comparable heat-flux spike appears on the windward side. The asymmetry can be interpreted using the curved-

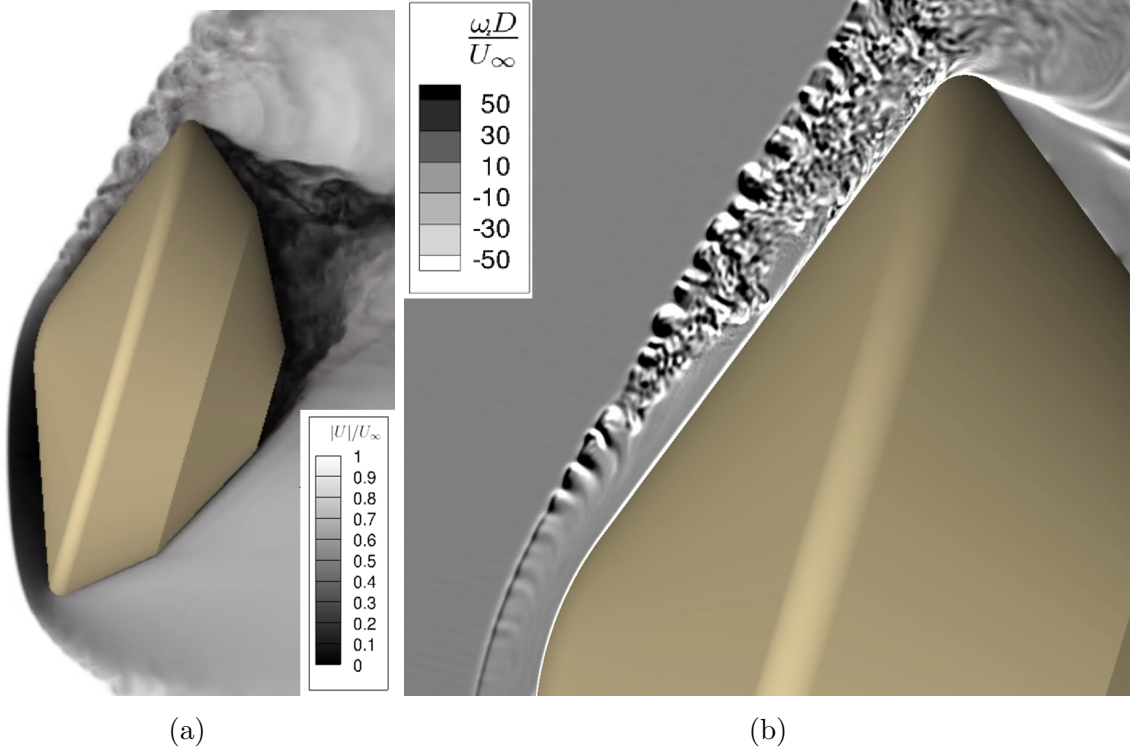


FIG. 14: WMLES of the MSL configuration at a representative point on the entry trajectory [10]. Freestream conditions from table I for a calorically perfect ideal gas with  $\gamma^* = 1.20$  at  $\alpha = 17.3^\circ$ . (a) Velocity magnitude. (b) Out-of-plane vorticity component. The view is focused on the leeside of the MSL heat shield.

shock vorticity scaling in (34), which shows that vorticity deposition increases with shock curvature, shock obliquity, and compression ratio. At this angle of attack, the leeside branch of the bow shock is more oblique and more strongly curved than the windward branch. The windward shock, by contrast, is closer to normal incidence and has smaller curvature. The leeside shock therefore generates a stronger shear–entropy layer, providing the energetic base state on which the amplification mechanism identified in §III C acts. This interpretation is also consistent with the high-density-ratio shock-layer instability picture of Hornung and Lemieux [38].

To connect the nonlinear calculation with the linear theory, a freestream-receptivity calculation was performed at the same freestream state and with the same constant- $\gamma^*$  gas model. The linear solver used in the preceding sections assumes an axisymmetric base flow, and hence cannot represent the full three-dimensional MSL flow at  $\alpha = 17.3^\circ$ . As discussed in §II A, an effective angle construction is used to match the local forebody inclination seen by the leeside flow, yielding a comparable shock obliquity and curvature along that branch, the two geometric factors entering (34). It does not reproduce the azimuthal curvature or the full three-dimensional shock shape, and the comparison should be understood as a test of the local instability mechanism rather than as a one-to-one reproduction of the complete MSL flow.

Figure 15 compares the out-of-plane vorticity from the early WMLES field with the leading linear freestream-receptivity response. The corresponding cycle-averaged gain is  $\overline{G}_T^{\text{opt}} =$

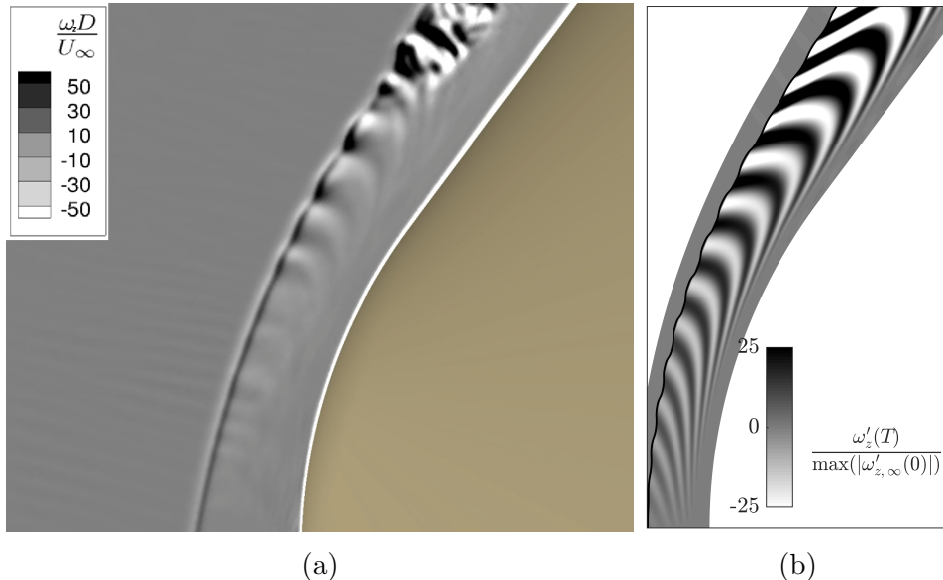


FIG. 15: Out-of-plane vorticity component in the incipient region of the instability. Comparison between the WMLES field and the leading freestream-receptivity response. Both calculations use the freestream conditions from table I and a calorically perfect ideal gas with  $\gamma^* = 1.20$ . The WMLES uses the actual MSL geometry at  $\alpha = 17.3^\circ$ ; the linear receptivity calculation uses an axisymmetric blunt cone with an effective half-angle of  $\theta = 52.7^\circ$ . (a) WMLES. (b) Linear freestream-receptivity response.

$4.92 \times 10^4$  for freestream receptivity. The leading linear response displays vortical structures in the same shock/shear-entropy-layer region as the incipient WMLES disturbance, before nonlinear saturation dominates.

Both approaches exhibit the same sequence of events: disturbances are generated in the region where the bow shock is curved, they are amplified while convecting through the shear-entropy layer, and they corrugate the shock as the pressure field couples back to the shock motion. Remarkably, the nonlinear WMLES displays the feedback mechanism anticipated from the analysis in §III D. Once the bow shock develops appreciable corrugation, the additional curvature visible in figure 15a injects further vorticity into the post-shock region. These streaks reinforce the local mean shear and feed the production term  $\mathcal{P}_u^k$  identified in §III B. This closes a finite-amplitude loop between shock corrugation, modified vorticity injection, mean-shear amplification, and disturbance growth. The WMLES result suggests that, beyond the linear regime, this self-reinforcing cycle can contribute to the rapid breakdown observed in the simulation and is a plausible candidate for the secondary instability pathway that precedes transition in this configuration.

#### IV. DISCUSSION

The heat-flux rise interpreted as leeside transition during the MSL entry occurred near  $Re_\infty = 2.85 \times 10^5$  [1, 10], well before the trajectory reached its maximum nose-radius Reynolds number,  $Re_\infty \simeq 8.8 \times 10^5$ , at approximately 85 seconds after atmospheric interface. By that later time, the abrupt leeside heat-flux spike had largely subsided and the measured

values were closer to the windside levels. This chronology does not rule out boundary-layer instability mechanisms, but it is difficult to reconcile with a transition criterion controlled primarily by  $Re_\infty$  or  $Re_\theta$  alone. The present results point instead to a gain scale that depends on Reynolds number through the finite- $Re_\infty$  viscous correction derived in §III C 2, namely

$$\mathcal{S}(Re_\infty, M_1, \gamma_2^*, \rho_2/\rho_1) = \gamma_2^* M_1^2 \exp\left[\frac{\rho_2/\rho_1}{C} - \frac{B}{\sqrt{Re_\infty}}\right],$$

where  $C$  and  $B$  are fixed, for the present geometry and disturbance family, by the scaling analysis of §III C. At the large Reynolds numbers relevant to the MSL transition point, the dominant trajectory dependence of  $\mathcal{S}$  is governed by  $M_1$ ,  $\gamma_2^*$  and the compression ratio  $\rho_2/\rho_1$ , rather than by  $Re_\infty$  alone. The fact that the maximum of this Mach–thermochemical gain scale occurs near the reconstructed MSL transition location and the corresponding Mars 2020/Perseverance velocity–altitude region supports the interpretation that the observed leeside event was influenced by the bow-shock/shear–entropy-layer receptivity mechanism identified here.

A separate question is whether the optimal freestream disturbances computed in the linear analysis are likely to be realized in free flight. The leading optimal mode should be interpreted as the most amplified member of an admissible disturbance space, and therefore as an upper bound on linear energy amplification. Real atmospheric disturbances will instead contain a broadband distribution of acoustic, entropic and vortical components with different projections onto the optimal input directions. Nevertheless, the present spectrum is not sharply isolated. At  $Re_\infty = 2.85 \times 10^5$  and the freestream conditions of table I, the first ten eigenvalues of the cycle-averaged gain operator have logarithmic cycle-averaged gains  $\bar{N}_j = \ln \bar{G}_{T,j}^\infty$  exceeding 11, and the first hundred have  $\bar{N}_j > 9.6$ , where the subscript  $j$  denotes the ordered optimal input. Thus the large amplification is not confined to a single precisely tuned disturbance. The linear calculation does not, by itself, set the absolute transition threshold; that threshold depends on the incident disturbance amplitudes, their spectral content, and the nonlinear breakdown process. It does show, however, that relatively small upstream acoustic and entropic components can be converted into a large post-shock response under the critical Mars-entry conditions.

The ground-test database used in the design and interpretation of MSL-class blunt capsules provides an important but nontrivial point of comparison. Experiments in AEDC Tunnel 9, CUBRC LENS facilities, Caltech T5, and the NASA Langley Mach 6 and Mach 10 tunnels reported transition and enhanced leeside heating on MSL/CEV-type geometries [5, 7–9, 11]. This database motivated the engineering smooth-body criterion  $Re_\theta \approx 200$  used in MSL design and subsequent blunt-body transition correlations [5, 10]. In terms of the present mechanism, however, the relevant inviscid part of the gain scale is

$$\mathcal{S}_0 = \gamma_2^* M_1^2 \exp\left(\frac{\rho_2/\rho_1}{C}\right),$$

with the finite-Reynolds-number correction supplied by the additional factor  $\exp[-B/\sqrt{Re_\infty}]$ . The values of  $\mathcal{S}_0$  in many of the ground-test conditions are one to two orders of magnitude smaller than those at the MSL and 2020/Perseverance flight points where enhanced leeside heating was reconstructed. This difference explains why a direct Reynolds-number extrapolation from tunnel data to flight can be misleading for this instability.

The lower gain scale in those facilities does not imply that the ground-test transition mea-

measurements are irrelevant. Rather, it means that the transition threshold in a facility depends on both the intrinsic amplification and the incident disturbance environment. These facilities are not quiet in the sense relevant to receptivity: their freestream disturbance spectra can contain acoustic radiation from turbulent wall boundary layers, driver- or nozzle-generated fluctuations, and other facility-dependent acoustic, vortical and entropic components [23]. Because the optimal inputs in the present receptivity analysis are primarily acoustic and entropic, a larger facility-noise level can compensate for a smaller value of  $\mathcal{S}_0$  and still trigger transition. The existing tunnel data should therefore be interpreted as evidence that MSL-class geometries are susceptible to leeside transition, but not as a direct measurement of the free-flight threshold. Future experiments aimed specifically at this mechanism would benefit from quiet or otherwise well-characterized freestream conditions, together with diagnostics of the incident acoustic and entropic spectra.

The projectile experiments of Hornung and Lemieux [38] are especially relevant in this context because they reduced the usual tunnel-wall noise pathway by launching a body into a quiescent test gas. Their propane cases were chosen to approach the Newtonian, high-compression limit, for which vibrational and chemical relaxation can produce large values of  $\rho_2/\rho_1$ . They reported two representative propane conditions: one at 2.26 km s<sup>-1</sup> with  $\rho_2/\rho_1 \simeq 13$ , and another at 2.70 km s<sup>-1</sup> with  $\rho_2/\rho_1 \simeq 20$ . Using the present inviscid gain scale and assuming  $C = 2.23$ , the ratio between the two cases is

$$\frac{\mathcal{S}_{0,2}}{\mathcal{S}_{0,1}} = \frac{\gamma_{2,2}^*}{\gamma_{2,1}^*} \left( \frac{M_{1,2}}{M_{1,1}} \right)^2 \exp \left[ \frac{(\rho_2/\rho_1)_2 - (\rho_2/\rho_1)_1}{C} \right].$$

If the upstream sound speed and post-shock effective specific-heat ratio are comparable between the two propane cases, this gives

$$\frac{\mathcal{S}_{0,2}}{\mathcal{S}_{0,1}} \approx \left( \frac{2.70}{2.26} \right)^2 \exp \left( \frac{20 - 13}{2.23} \right) \simeq 33.$$

This estimate is consistent with the qualitative experimental observation that the higher-compression case developed a much more disturbed shock layer, including visible shock oscillations in the schlieren images. Similar shock corrugation appears in the present linear receptivity calculation and in the early stages of the WMLES solution in figure 15.

## V. CONCLUSIONS

The Mars Science Laboratory and Perseverance entries exhibited localized leeside heating increases that are consistent with transition and remain difficult to predict with existing blunt-body transition criteria [1, 2, 6]. This study investigated a candidate mechanism for those events by combining shock-fitted freestream receptivity analysis, energy-budget diagnostics, scaling arguments, velocity–altitude gain maps, and wall-modeled large-eddy simulations. The central result is that, under high-enthalpy Mars-entry conditions, the detached bow shock and the post-shock shear–entropy layer constitute a high-gain receptivity pathway through which linear mechanisms amplify freestream disturbances by orders of magnitude. These amplified disturbances corrugate the bow shock, establishing a feedback mechanism that further drives the instability. Corresponding nonlinear simulations show that the result-

ing shock-layer response can evolve toward breakdown and localized heating.

The optimal freestream inputs are dominated by acoustic and entropic components, with only a small kinetic contribution. This preference is consistent with classical linear interaction theory: in the strong-shock limit, acoustic and entropic incident disturbances produce transmitted thermodynamic and energy-flux perturbations that increase as  $\mathcal{O}(M_1^2)$ , whereas the kinetic-energy-containing vortical component is not amplified by the same Mach-number factor [14, 15]. The bow shock therefore acts as a selective amplifier of the disturbance components that are most effective at forcing the post-shock layer. The curved shock also deposits vorticity and entropy gradients [33], creating the shear–entropy layer in which the downstream amplification occurs.

The physical mechanism can be summarized as a three-step process. First, the incoming acoustic and entropic components are amplified as they cross the fitted bow shock. Second, the transmitted disturbance packet enters the post-shock shear–entropy layer and extracts energy from the base flow. The dominant kinetic-energy production is the Reynolds-stress work against the mean shear  $\mathcal{P}_u^k$ , while the accompanying entropy gradient produces the leading entropic source term,  $\mathcal{P}_u^s$ . Third, the amplified disturbance field perturbs and corrugates the bow shock, closing the shock-layer feedback. For the open-loop linear gain, the scaling reduces to two multiplicative factors: shock transmission and post-shock convective amplification. The corresponding cycle-averaged asymptotic gain scale is

$$\overline{G}_T^{\text{opt}} \sim \gamma_2^* M_1^2 \exp \left[ \frac{\rho_2/\rho_1}{C} - \frac{B}{\sqrt{Re_\infty}} \right],$$

with  $C = 2.23$  and  $B = 685$  for the present geometry and class of optimal disturbance paths. This expression retains the inviscid Mach-number and thermochemical dependence through  $\gamma_2^* M_1^2 \exp[(\rho_2/\rho_1)/C]$ , while also including the leading viscous correction inferred from the Reynolds-number sweep.

At the representative Mars-entry condition, the computed optimal total gains are of order  $10^6$  ( $\overline{G}_T^{\text{opt}} = 7.9 \times 10^5$  and  $G_{T,\text{max}}^{\text{opt}} = 9.7 \times 10^5$  in the baseline case). In the energy-gain convention used here,  $N \equiv \ln \overline{G}$ , these values correspond to  $N \simeq 14$ . The velocity–altitude maps show that the largest values of the gain scale occur near the reconstructed MSL transition point and in the same region of velocity–altitude space where Mars 2020/Perseverance reconstructions also indicate transition-associated heat-flux augmentation. By contrast, Earth-entry conditions produce substantially smaller values of the same scale because the lower compression ratios and lower Mach numbers reduce both the shock transmission and post-shock convective amplification. This comparison supports the interpretation that the observed Mars-entry behavior is not controlled by Reynolds number alone, but by the coupled dependence on Mach number, thermochemistry and shock-layer compression.

The nonlinear WMLES calculations provide an independent consistency check on the linear mechanism. In the MSL geometry at representative Mars-entry conditions, reducing the effective specific-heat ratio  $\gamma^*$  increases the post-shock compression ratio and hence the gain scale. The simulations then develop strong shear–entropy-layer disturbances on the leeside, followed by nonlinear breakdown and a localized heat-flux spike. The location and flow topology of this breakdown are qualitatively consistent with the flight heat-flux reconstructions and with the leading structures predicted by the linear receptivity analysis.

Overall, the study identifies a bow-shock-mediated transition route for high-enthalpy blunt-body entry flows. The mechanism is distinct from classical wall-localized boundary-

layer routes: the dominant amplification begins at the shock and in the outer post-shock shear–entropy layer, and only later leads to near-wall turbulent heating. The resulting scaling provides a compact, physically interpretable gain indicator for identifying regimes in which this pathway is likely to be important. Its use in thermal-protection-system design should be paired with estimates of the freestream disturbance environment and with additional validation across capsule geometries, wall thermal conditions and thermochemical models.

### **ACKNOWLEDGEMENTS**

The authors gratefully acknowledge Professor Hans G. Hornung for valuable discussions on entropy layer instabilities. We also thank Professor Joseph E. Shepherd for generously sharing thermochemical data files.

### **FUNDING**

This work is supported by an Early Career Faculty grant from NASA’s Space Technology Research Grants Program (grant #80NSSC23K1498).

### **DECLARATION OF INTERESTS**

The authors report no conflict of interest.

### **AUTHOR ORCIDS**

A. Antón-Álvarez, <https://orcid.org/0000-0002-6434-4211>;  
A. Lozano-Durán, <https://orcid.org/0000-0001-9306-0261>

- 
- [1] D. Bose, T. White, M. Mahzari, and K. Edquist, Reconstruction of aerothermal environment and heat shield response of Mars Science Laboratory, *J. Spacecraft Rockets* **51**, 1174 (2014).
  - [2] K. T. Edquist, M. Mahzari, and H. Alpert, Mars 2020 reconstructed aerothermal environments and design margins, in *AIAA SciTech 2022 Forum* (2022) aIAA Paper 2022-0553.
  - [3] S. P. Schneider, Hypersonic laminar–turbulent transition on circular cones and scramjet forebodies, *Prog. Aerosp. Sci.* **40**, 1 (2004).
  - [4] E. V. Zoby, J. N. Moss, and K. Sutton, Approximate convective-heating equations for hypersonic flows, *J. Spacecraft Rockets* **18**, 64 (1981).
  - [5] B. Hollis, Blunt-body entry vehicle aerothermodynamics: transition and turbulence on the CEV and MSL configurations, in *40th AIAA Fluid Dynamics Conference and Exhibit* (2010) aIAA Paper 2010-4984.
  - [6] H. Alpert, M. Mahzari, D. Saunders, J. Monk, and T. R. White, Inverse estimation of Mars 2020 entry aeroheating environments using MEDLI2 flight data, in *AIAA SciTech 2022 Forum* (2022) aIAA Paper 2022-0550.
  - [7] B. Hollis, D. Liechty, M. Wright, M. Holden, T. Wadhams, M. MacLean, and A. Dyakonov, Transition onset and turbulent heating measurements for the Mars Science Laboratory entry vehicle, in *43rd AIAA Aerospace Sciences Meeting and Exhibit* (2005) aIAA Paper 2005-1437.
  - [8] B. Hollis and A. Collier, Turbulent aeroheating testing of Mars Science Laboratory entry vehicle in perfect-gas nitrogen, in *45th AIAA Aerospace Sciences Meeting and Exhibit* (2007) aIAA Paper 2007-1208.
  - [9] D. S. Liechty, B. R. Hollis, and K. T. Edquist, Mars Science Laboratory experimental aerothermodynamics with effects of cavities and control surfaces, *J. Spacecraft Rockets* **43**, 340 (2006).
  - [10] K. Edquist, A. Dyakonov, M. Wright, and C. Tang, Aerothermodynamic environments definition for the Mars Science Laboratory entry capsule, in *45th AIAA Aerospace Sciences Meeting and Exhibit* (2007) aIAA Paper 2007-1206.
  - [11] M. J. Wright, J. Olejniczak, J. L. Brown, H. G. Hornung, and K. T. Edquist, Modeling of shock tunnel aeroheating data on the Mars Science Laboratory aeroshell, *J. Thermophys. Heat Transfer* **20**, 641 (2006).
  - [12] J. Laufer, Factors affecting transition Reynolds numbers on models in supersonic wind tunnels, *J. Aeronaut. Sci.* **21**, 497 (1954).
  - [13] J. M. Kendall, Wind tunnel experiments relating to supersonic and hypersonic boundary-layer transition, *AIAA J.* **13**, 290 (1975).
  - [14] J. F. McKenzie and K. O. Westphal, Interaction of linear waves with oblique shock waves, *Phys. Fluids* **11**, 2350 (1968).
  - [15] H. S. Ribner, *Convection of a pattern of vorticity through a shock wave*, Tech. Rep. TN-2864 (NACA, 1954).
  - [16] J. Larsson and S. K. Lele, Direct numerical simulation of canonical shock/turbulence interaction, *Phys. Fluids* **21**, 126101 (2009).
  - [17] A. V. Fedorov and A. P. Khokhlov, Prehistory of instability in a hypersonic boundary layer, *Theor. Comput. Fluid Dyn.* **14**, 359 (2001).
  - [18] A. V. Fedorov, Receptivity of a high-speed boundary layer to acoustic disturbances, *J. Fluid Mech.* **491**, 101 (2003).

- [19] Y. Ma and X. Zhong, Receptivity of a supersonic boundary layer over a flat plate. Part 1. Wave structures and interactions, *J. Fluid Mech.* **488**, 31 (2003).
- [20] Y. Ma and X. Zhong, Receptivity of a supersonic boundary layer over a flat plate. Part 2. Receptivity to free-stream sound, *J. Fluid Mech.* **488**, 79 (2003).
- [21] F. Qin and X. Wu, Response and receptivity of the hypersonic boundary layer past a wedge to free-stream acoustic, vortical and entropy disturbances, *J. Fluid Mech.* **797**, 874 (2016).
- [22] O. Kamal, M. T. Lakebrink, and T. Colonius, Global receptivity analysis: physically realizable input–output analysis, *J. Fluid Mech.* **956**, R5 (2023).
- [23] S. P. Schneider, Effects of high-speed tunnel noise on laminar–turbulent transition, *J. Spacecraft Rockets* **38**, 323 (2001).
- [24] A. Antón-Álvarez and A. Lozano-Durán, HYMOR: an open-source package for global modal, non-modal, and receptivity analysis in high-enthalpy hypersonic vehicles, arXiv:2604.03824 (2026).
- [25] D. G. Goodwin, H. K. Moffat, I. Schoegl, R. L. Speth, and B. W. Weber, Cantera: an object-oriented software toolkit for chemical kinetics, thermodynamics, and transport processes, <https://www.cantera.org> (2024), version 3.1.0.
- [26] C. R. Wilke, A viscosity equation for gas mixtures, *J. Chem. Phys.* **18**, 517 (1950).
- [27] E. A. Mason and S. C. Saxena, Approximate formula for the thermal conductivity of gas mixtures, *Phys. Fluids* **1**, 361 (1958).
- [28] T. J. Poinso and S. K. Lele, Boundary conditions for direct simulations of compressible viscous flows, *J. Comput. Phys.* **101**, 104 (1992).
- [29] M. Pandolfi and D. D’Ambrosio, Numerical instabilities in upwind methods: analysis and cures for the “carbuncle” phenomenon, *J. Comput. Phys.* **166**, 271 (2001).
- [30] A. Antón-Álvarez and A. Lozano-Durán, Bow shockwave instabilities of the Mars Science Laboratory using wall-modeled large eddy simulation, in *AIAA SciTech 2025 Forum* (2025) aIAA Paper 2025-2259.
- [31] L. M. Mack, *Boundary-layer linear stability theory*, Tech. Rep. Report 709 (AGARD, 1984) special Course on Stability and Transition of Laminar Flows.
- [32] P. J. Schmid and D. S. Henningson, *Stability and Transition in Shear Flows*, Vol. 142 (Springer, 2012).
- [33] H. G. Hornung, Gradients at a curved shock in reacting flow, *Shock Waves* **8**, 11 (1998).
- [34] R. Manders, *Apollo 11 entry postflight analysis*, Tech. Rep. MSC Internal Note 70-FM-30 (NASA Manned Spacecraft Center, Houston, Texas, 1970) nASA-TM-X-69419.
- [35] A. W. Vreman, An eddy-viscosity subgrid-scale model for turbulent shear flow: algebraic theory and applications, *Phys. Fluids* **16**, 3670 (2004).
- [36] S. Kawai and J. Larsson, Wall-modeling in large eddy simulation: length scales, grid resolution, and accuracy, *Phys. Fluids* **24**, 015105 (2012).
- [37] G. K. Batchelor, *An Introduction to Fluid Dynamics* (Cambridge University Press, 2000).
- [38] H. G. Hornung and P. Lemieux, Shock layer instability near the Newtonian limit of hypervelocity flows, *Phys. Fluids* **13**, 2394 (2001).
- [39] J. E. Shepherd, Chemical reaction and thermodynamic data – Cantera format, Explosion Dynamics Laboratory, California Institute of Technology, [https://shepherd.caltech.edu/EDL/PublicResources/sdt/cti\\_mech.html](https://shepherd.caltech.edu/EDL/PublicResources/sdt/cti_mech.html) (2023), accessed: 2025-01-17.
- [40] R. C. Millikan and D. R. White, Systematics of vibrational relaxation, *J. Chem. Phys.* **39**, 3209 (1963).

- [41] I. Armenise and E. Kustova, Effect of asymmetric mode on CO<sub>2</sub> state-to-state vibrational–chemical kinetics, *J. Phys. Chem. A* **122**, 8709 (2018).
- [42] NASA Glenn Research Center, Mars atmosphere model – metric units, <https://www.grc.nasa.gov/WWW/K-12/airplane/atmosmrm.html> (2021).
- [43] NOAA, NASA and USAF, *U.S. Standard Atmosphere*, Tech. Rep. NASA-TM-X-74335 (U.S. Government Printing Office, 1976).
- [44] P. Sagaut and C. Cambon, *Homogeneous Turbulence Dynamics* (Springer, 2008).

## Appendix A: Validity of thermochemical models

This appendix assesses the range of Mars- and Earth-entry conditions for which the equilibrium assumptions introduced in §II B 2 are valid. We first examine the chemical- and thermal-equilibration time scales. Equilibrium models presume that the characteristic times of chemical relaxation and internal-energy relaxation are small compared with the flow time scales of interest. We therefore examine finite-rate chemistry and vibrational relaxation. Electronic excitation is not assigned a separate relaxation time in the present estimates, because its contribution is negligible over the temperature range considered here; when it is present in the equilibrium thermodynamic database, it is included only in the combined vibrational–electronic energy bookkeeping below.

The chemical relaxation time  $\tau_{\text{chem}}$  is defined here as an effective one-time-scale measure of the approach of a reacting mixture to its local equilibrium composition. We use the departure of the translational–rotational energy from its equilibrium value as a scalar progress variable. Assuming first-order relaxation,

$$\frac{e_{T-R}(t) - e_{T-R}^{\text{eq}}}{e_{T-R}(0) - e_{T-R}^{\text{eq}}} = \exp\left(-\frac{t}{\tau_{\text{chem}}}\right). \quad (\text{A1})$$

The relaxation time  $\tau_{\text{chem}}$  is recovered from the time  $t_5$  at which the normalized departure from equilibrium first falls to 5%:

$$\left. \frac{e_{T-R}(t) - e_{T-R}^{\text{eq}}}{e_{T-R}(0) - e_{T-R}^{\text{eq}}} \right|_{t=t_5} = 0.05 \quad \implies \quad \tau_{\text{chem}}(P, T, \mathbf{X}) = -\frac{t_5}{\ln(0.05)}. \quad (\text{A2})$$

We obtain  $t_5$  by integrating an adiabatic, constant-pressure reactor in Cantera [25], using the thermochemical data set of Shepherd [39], from the initial state  $(P, T, \mathbf{X})$  and recording the first crossing of the 5% threshold.

The vibrational relaxation time  $\tau_{\text{vib}}$  is estimated from the Millikan–White correlation [40]. For the Earth-atmosphere cases, we use the dominant self-collision relaxation of  $\text{N}_2$ , with  $\theta = 3350$  K and  $\mu_{\text{N}_2\text{-N}_2}^{\text{red}} = 14$  g mol<sup>-1</sup>. For the Mars-atmosphere cases,  $\text{CO}_2$  is dominant but has three characteristic vibrational frequencies and four vibrational degrees of freedom. As a conservative estimate of the slowest relaxation process, we use the asymmetric stretching mode, with  $\theta = 3380$  K and  $\mu_{\text{CO}_2\text{-CO}_2}^{\text{red}} = 22$  g mol<sup>-1</sup>. This dominant-species approximation neglects mixture corrections to vibrational relaxation and is less accurate for polyatomic molecules than for diatomic nitrogen; the latter limitation is well documented for  $\text{CO}_2$  kinetics [41].

Computing the chemical and vibrational relaxation times requires an estimate of the post-shock state  $(P, T, \mathbf{X})$ . Although the actual post-shock state varies along the curved bow shock, we use the state immediately downstream of the corresponding normal shock as a stagnation-line estimate. This construction should therefore be interpreted as an order-of-magnitude criterion for the forebody shock layer. Across the shock, vibrational excitation, electronic excitation and chemical reactions are assumed frozen, while translational and rotational modes are taken to be equilibrated. The composition is therefore equal to the freestream composition immediately behind the shock. Under these assumptions, the jump conditions reduce to the Rankine–Hugoniot relations for a calorically perfect gas with  $\gamma_{T-R} = 1 + R_g/c_{v,T-R}$ .

Next, we assess the validity of the calorically perfect gas approximation. Starting from the frozen post-shock Rankine–Hugoniot (RH) state, we compute the corresponding equilibrium state with Cantera [25] and the thermochemical data set of Shepherd [39]. The equilibrium state used to define  $E_R$  is obtained at fixed density and fixed specific internal energy. The fraction of the frozen post-shock translational–rotational thermal energy transferred to vibrational–electronic and chemical energy storage during this relaxation quantifies the departure from calorically perfect behavior.

Assuming translational–rotational equipartition, the specific translational–rotational energy is

$$e_{T-R} = c_{v,T-R}T, \quad \frac{c_{v,T-R}}{R_u} = \frac{1}{W} \sum_i X_i \frac{Z_i}{2}, \quad (\text{A3})$$

where  $R_u$  is the universal gas constant,  $X_i$  are mole fractions,  $W = \sum_i X_i W_i$  is the mixture molar mass, with all molar masses expressed in consistent units, and  $Z_i$  is the number of active translational–rotational degrees of freedom of species  $i$ .

Because vibrational excitation, electronic excitation and chemical reactions are frozen across the shock, the shock-generated thermal energy initially resides in the translational–rotational pool,  $e_{T-R}^{\text{RH}}$ . We therefore normalize the redistributed energy by  $e_{T-R}^{\text{RH}}$ . Conservation of total internal energy during the fixed-density relaxation implies  $\Delta e_{T-R} = -\Delta(e_{V-E} + e_{\text{chem}})$ , so the relaxed energy fraction is

$$\begin{aligned} E_R &\equiv \frac{e_{T-R}^{\text{RH}} - e_{T-R}^{\text{eq}}}{e_{T-R}^{\text{RH}}} = \frac{\Delta(e_{V-E} + e_{\text{chem}})}{e_{T-R}^{\text{RH}}} \\ &= \frac{\frac{T^{\text{RH}}}{W^{\text{RH}}} \sum_i X_i^{\text{RH}} \frac{Z_i}{2} - \frac{T^{\text{eq}}}{W^{\text{eq}}} \sum_i X_i^{\text{eq}} \frac{Z_i}{2}}{\frac{T^{\text{RH}}}{W^{\text{RH}}} \sum_i X_i^{\text{RH}} \frac{Z_i}{2}}. \end{aligned} \quad (\text{A4})$$

Thus,  $E_R$  represents the fraction of the frozen post-shock translational–rotational thermal energy that is redistributed to vibrational–electronic and chemical modes at equilibrium. Mass-specific energies are used throughout because the number of moles is not conserved during chemical reactions, whereas mass is.

The vibrational relaxation time  $\tau_{\text{vib}}$ , chemical relaxation time  $\tau_{\text{chem}}$ , and energy-relaxation fraction  $E_R$  are shown in figures 16a and 16b for the Earth and Mars atmospheres, respectively. The Martian atmosphere is modeled following NASA Glenn Research Center [42], while the Earth atmosphere is modeled using the U.S. Standard Atmosphere [43]. The first observation is that the calorically perfect gas approximation remains valid to higher velocities in the Earth atmosphere than in the Martian atmosphere. In the Martian atmosphere, contributions to  $E_R$  become significant at lower velocities because the dominant species,  $\text{CO}_2$ , activates vibrational-energy storage at lower temperatures than  $\text{N}_2$ . For example, over the altitude range shown, Earth-entry states with velocities below approximately  $2000 \text{ m s}^{-1}$  have  $E_R \lesssim 10\%$ , so a calorically perfect model is often reasonable. In the Martian atmosphere, states near  $2000 \text{ m s}^{-1}$  can have  $E_R$  of order 40% over the same range, indicating that vibrational and chemical energy storage may already be important. In particular, excitation of the  $\text{CO}_2$  bending mode provides the dominant contribution to  $E_R$  at lower velocities because this mode has a low characteristic vibrational temperature.

Regarding the chemical and thermal equilibrium assumptions, the relaxation times must be compared with a representative residence time of the gas in the shock layer. The chemical and vibrational relaxation times in the Earth-atmosphere cases are much shorter than in the Martian cases over most of the plotted range, primarily because the post-shock Earth-atmosphere states are denser and molecular collisions are therefore more frequent. To compare relaxation and flow time scales along representative trajectories, we consider the Apollo 11 Earth re-entry trajectory [34] and the MSL Mars-entry trajectory [10]. We define a body-scale post-shock flow time

$$\tau_{\text{flow}} = \frac{R}{U_2^{\text{RH}}}, \quad (\text{A5})$$

where  $R$  is the capsule nose radius and  $U_2^{\text{RH}}$  is the post-shock velocity from the corresponding normal-shock Rankine–Hugoniot estimate. This gives

$$Da_{\text{chem}} = \frac{\tau_{\text{flow}}}{\tau_{\text{chem}}}, \quad Da_{\text{vib}} = \frac{\tau_{\text{flow}}}{\tau_{\text{vib}}}. \quad (\text{A6})$$

These Damköhler numbers, together with the Apollo 11 and MSL trajectories, are shown in figure 17.

For the Earth-entry case, figure 17a shows that, for velocities above approximately  $2500 \text{ m s}^{-1}$ , vibrational and chemical relaxation are much faster than the body-scale flow time, so thermal and chemical equilibrium are reasonable approximations. At higher altitudes and velocities near  $2000 \text{ m s}^{-1}$ , the relaxation times become comparable to the flow time. In that regime, however,  $E_R$  is less than 10%, so the departure from a calorically perfect gas remains small. We therefore infer that thermal and chemical equilibrium are reasonable approximations along the Apollo 11 re-entry trajectory over the range considered here.

We next consider the MSL entry into the Martian atmosphere (figure 17b). For velocities around  $3000 \text{ m s}^{-1}$ , the chemical and vibrational relaxation times start to become comparable to the body-scale flow time. In this regime,  $E_R$  remains substantial, with values of order 50%, so thermochemical nonequilibrium should be retained for accurate aerothermodynamic modeling. Of this energy fraction, most of the energy is transferred to vibrational degrees of freedom for post-shock temperatures below approximately 3000 K. Although vibrational relaxation is faster than chemical relaxation,  $Da_{\text{vib}}$  is already of order unity near  $2000 \text{ m s}^{-1}$ , so thermal nonequilibrium cannot be neglected there. At higher velocities,  $U_\infty > 4000 \text{ m s}^{-1}$ , the equilibrium approximation becomes increasingly appropriate, especially for vibrational relaxation. This high-velocity region is the most relevant one for the present stability analysis, because it overlaps the portion of the Mars-entry trajectories where large aeroheating rates and transition-associated heat-flux augmentation are reported [1, 2].

The critical Mars-entry region in which transition-associated heating was inferred for MSL and Mars 2020/Perseverance, and from which the representative state in table I is drawn, corresponds to velocities above  $5000 \text{ m s}^{-1}$  and altitudes near 30 km. In this regime, the Damköhler numbers in the Martian atmosphere (figure 17b) lie in the ranges  $Da_{\text{vib}} \approx 10^4\text{--}10^5$  and  $Da_{\text{chem}} \approx 10^2\text{--}10^3$ . The relaxation times are therefore short compared with the body-scale residence time, supporting the use of thermochemical equilibrium in the stability calculations, although chemical relaxation remains slower than vibrational relaxation. As a check, several computations were performed within the critical gain region using the finite-rate chemistry model developed in Antón-Álvarez and Lozano-Durán [24], and no changes in

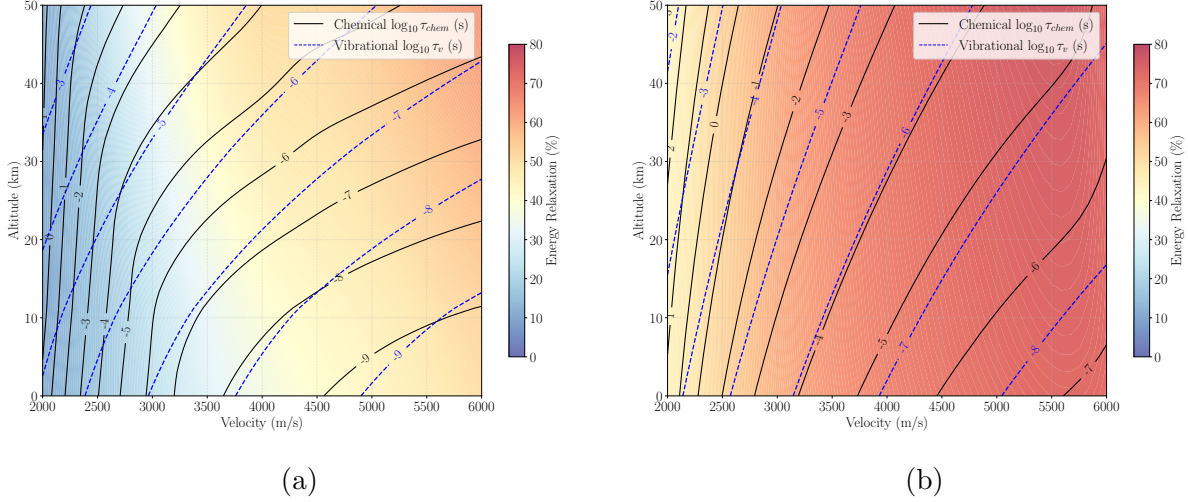


FIG. 16: Chemical and vibrational relaxation times for Earth and Mars atmospheres. Contours are shown as  $\log_{10}(\tau/s)$ . The background color shows the energy-relaxation fraction  $E_R$ , expressed as a percentage of the frozen post-shock translational–rotational thermal energy. (a) Earth atmosphere:  $X_{N_2} = 0.7812$ ,  $X_{O_2} = 0.2095$ ,  $X_{Ar} = 0.0093$ . (b) Mars atmosphere:  $X_{CO_2} = 0.9556$ ,  $X_{N_2} = 0.0270$ ,  $X_{Ar} = 0.0160$ ,  $X_{O_2} = 0.0014$ .

the optimal gains were found at a level that would affect the conclusions. These computations were, however, considerably more expensive: the thin thermochemical relaxation layer immediately behind the shock, in which translational–rotational energy is redistributed into vibrational, electronic and chemical energy modes, required a much finer local grid and a correspondingly smaller time step. Given the substantial increase in computational cost and the negligible impact on the amplification factors, thermochemical equilibrium was adopted throughout the subsequent analysis.

## Appendix B: Energy budgets

This appendix derives the transport equations for the kinetic and entropic contributions to Chu’s norm. Acoustic energy is omitted because it plays no leading role in the cases analyzed in the main text.

We decompose the flow variables into a steady base state and infinitesimal perturbations,

$$\begin{aligned}
 \rho &= \rho_0 + \rho', & |\rho'| &\ll \rho_0, \\
 u_i &= u_{i,0} + u'_i, & |u'_i| &\ll |u_{i,0}|, \\
 p &= p_0 + p', & |p'| &\ll p_0, \\
 T &= T_0 + T', & |T'| &\ll T_0, \\
 s &= s_0 + s', & |s'| &\ll s_0,
 \end{aligned}$$

where  $\rho$ ,  $u_i$ ,  $p$ ,  $T$ , and  $s$  denote density, velocity, pressure, temperature, and entropy, respectively. The base flow is steady, so  $\partial(\cdot)_0/\partial t = 0$ .

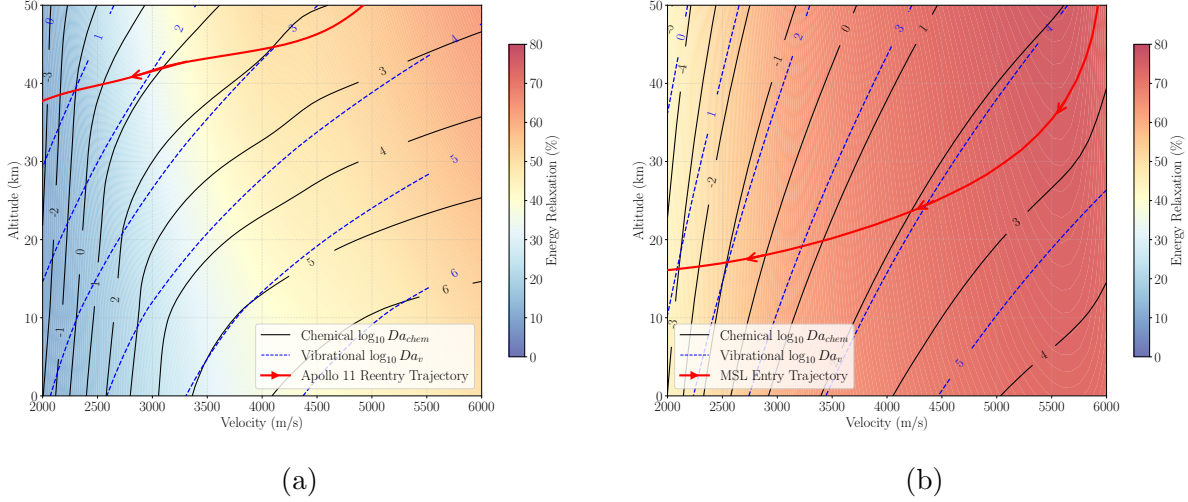


FIG. 17: Contour lines show Damköhler numbers for Earth and Mars atmospheres as  $\log_{10}(Da)$ . Red curves indicate the Apollo 11 Earth re-entry trajectory and the MSL Mars-entry trajectory. The background color shows the energy-relaxation fraction  $E_R$ , expressed as a percentage of the frozen post-shock translational-rotational thermal energy. (a) Earth atmosphere:  $X_{N_2} = 0.7812$ ,  $X_{O_2} = 0.2095$ ,  $X_{Ar} = 0.0093$ . (b) Mars atmosphere:  $X_{CO_2} = 0.9556$ ,  $X_{N_2} = 0.0270$ ,  $X_{Ar} = 0.0160$ ,  $X_{O_2} = 0.0014$ .

### 1. Kinetic energy budget

The kinetic contribution to Chu's norm is

$$E^k = \int \frac{1}{2} \rho_0 u'_i u'_i dV.$$

Retaining terms up to second order in the perturbation amplitudes gives the familiar compressible kinetic-energy budget [44],

$$\rho_0 \frac{\partial}{\partial t} \left( \frac{1}{2} u'_i u'_i \right) = \mathcal{A}^k + \mathcal{P}^k + \Pi_d^k + \mathcal{T}^k + \mathcal{D}^k, \quad (\text{B1})$$

where

- Advection:

$$\mathcal{A}^k = -\rho_0 u_{j,0} \frac{\partial}{\partial x_j} \left( \frac{1}{2} u'_i u'_i \right),$$

- Production:

$$\mathcal{P}^k = -\rho_0 u'_i u'_j \frac{\partial u_{i,0}}{\partial x_j} - \rho' u'_i u_{j,0} \frac{\partial u_{i,0}}{\partial x_j},$$

which represents transfer from the mean flow to the perturbations.

- Pressure–dilatation:

$$\Pi_d^k = p' \frac{\partial u'_i}{\partial x_i},$$

- Transport:

$$\mathcal{T}^k = \frac{\partial}{\partial x_j} (-u'_j p' + u'_i \tau'_{ij}),$$

- Dissipation:

$$\mathcal{D}^k = -\tau'_{ij} \frac{\partial u'_i}{\partial x_j}.$$

The linearized viscous stress is

$$\tau'_{ij} = \frac{1}{Re_\infty} \left[ \mu^{*'} \left( \frac{\partial u_{i,0}}{\partial x_j} + \frac{\partial u_{j,0}}{\partial x_i} - \frac{2}{3} \delta_{ij} \frac{\partial u_{k,0}}{\partial x_k} \right) + \mu_0^* \left( \frac{\partial u'_i}{\partial x_j} + \frac{\partial u'_j}{\partial x_i} - \frac{2}{3} \delta_{ij} \frac{\partial u'_k}{\partial x_k} \right) \right].$$

## 2. Entropic energy budget

The entropic contribution to Chu's norm is

$$E^s = \int \frac{(\gamma_0^* - 1)p_0}{2\gamma_0^*} \left( \frac{s'}{R_{g,0}} \right)^2 dV.$$

To obtain its transport equation, we start from the entropy equation for a viscous compressible flow,

$$\rho T \frac{Ds}{Dt} = -\frac{\partial q_j}{\partial x_j} + \Phi, \quad (\text{B2})$$

where the heat flux is

$$q_j = -k \frac{\partial T}{\partial x_j},$$

and the Rayleigh dissipation function is

$$\Phi = \tau_{ij} \frac{\partial u_i}{\partial x_j} = \mu \left( \frac{\partial u_i}{\partial x_j} + \frac{\partial u_j}{\partial x_i} - \frac{2}{3} \delta_{ij} \frac{\partial u_k}{\partial x_k} \right) \frac{\partial u_i}{\partial x_j}.$$

Linearizing (B2) about the steady base flow gives

$$\rho_0 T_0 \left( \frac{\partial s'}{\partial t} + u_{j,0} \frac{\partial s'}{\partial x_j} \right) + (\rho_0 T_0 u'_j + \rho' T_0 u_{j,0} + \rho_0 T' u_{j,0}) \frac{\partial s_0}{\partial x_j} = -\frac{\partial q'_j}{\partial x_j} + \Phi'.$$

Multiplying by  $s'$  and rearranging yields

$$\rho_0 T_0 \left[ \frac{\partial}{\partial t} \left( \frac{s'^2}{2} \right) + u_{j,0} \frac{\partial}{\partial x_j} \left( \frac{s'^2}{2} \right) \right] = -(\rho_0 T_0 u'_j + \rho' T_0 u_{j,0} + \rho_0 T' u_{j,0}) s' \frac{\partial s_0}{\partial x_j} - \frac{\partial}{\partial x_j} (s' q'_j) + \frac{\partial s'}{\partial x_j} q'_j + s' \Phi'.$$

Scaling this result to match Chu's norm gives

$$\frac{(\gamma_0^* - 1)p_0}{2\gamma_0^*} \frac{\partial}{\partial t} \left( \frac{s'^2}{R_{g,0}^2} \right) = \mathcal{A}^s + \mathcal{P}^s + \mathcal{T}^s + \mathcal{D}^s + \mathcal{S}^s, \quad (\text{B3})$$

where

- Advection:

$$\mathcal{A}^s = -\frac{(\gamma_0^* - 1)p_0}{\gamma_0^* R_{g,0}^2} u_{j,0} \frac{\partial}{\partial x_j} \left( \frac{s'^2}{2} \right),$$

- Production:

$$\mathcal{P}^s = -\frac{(\gamma_0^* - 1)p_0}{\gamma_0^* R_{g,0}^2} \left( u'_j + \frac{\rho'}{\rho_0} u_{j,0} + \frac{T'}{T_0} u_{j,0} \right) s' \frac{\partial s_0}{\partial x_j},$$

which contains velocity-, density-, and temperature-induced production.

- Transport:

$$\mathcal{T}^s = -\frac{(\gamma_0^* - 1)}{\gamma_0^* R_{g,0}} \frac{\partial}{\partial x_j} (s' q'_j),$$

- Dissipation:

$$\mathcal{D}^s = \frac{(\gamma_0^* - 1)}{\gamma_0^* R_{g,0}} \left( \frac{\partial s'}{\partial x_j} q'_j \right),$$

- Source:

$$\mathcal{S}^s = \frac{(\gamma_0^* - 1)}{\gamma_0^* R_{g,0}} (s' \Phi').$$

### Appendix C: Additional details on Reynolds-number dependence

The underlying mechanics of the scaling in the downstream region are tied to the viscous dissipation of the optimal disturbances. Since dissipation scales as  $k^2$ , where  $k$  is the disturbance wavenumber, higher Reynolds numbers support the sustenance of higher-frequency freestream disturbances for which viscous terms remain negligible. This effect is evident in figure 18, which reveals that the characteristic frequency of the optimal disturbance increases noticeably between  $Re_\infty = 20\,000$  and  $Re_\infty = 100\,000$ , enabling high-frequency excitation of both the shock and the entropy layer.

To further clarify the physical mechanisms underlying these Reynolds number scalings, the most relevant terms of the kinetic energy budgets are compared in figure 19 for  $Re_\infty = 20\,000$  and  $Re_\infty = 100\,000$ . At  $Re_\infty = 20\,000$ , viscous dissipation  $\mathcal{D}^k$  constitutes a significant contribution to the budget, directly competing with production and limiting the net energy growth. As the Reynolds number increases, dissipation diminishes in magnitude; however, the decrease is more gradual than one might anticipate on the basis of Reynolds number scaling alone. The reason is that the characteristic frequency of the optimal disturbance also increases with  $Re_\infty$  (as shown in figure 18), which partially offsets the reduction in viscous effects by introducing finer spatial scales that are more susceptible to dissipation.

Despite this frequency shift, Reynolds stress production  $\mathcal{P}_u^k$  remains the dominant source term in the kinetic energy budget at all Reynolds numbers investigated. This production

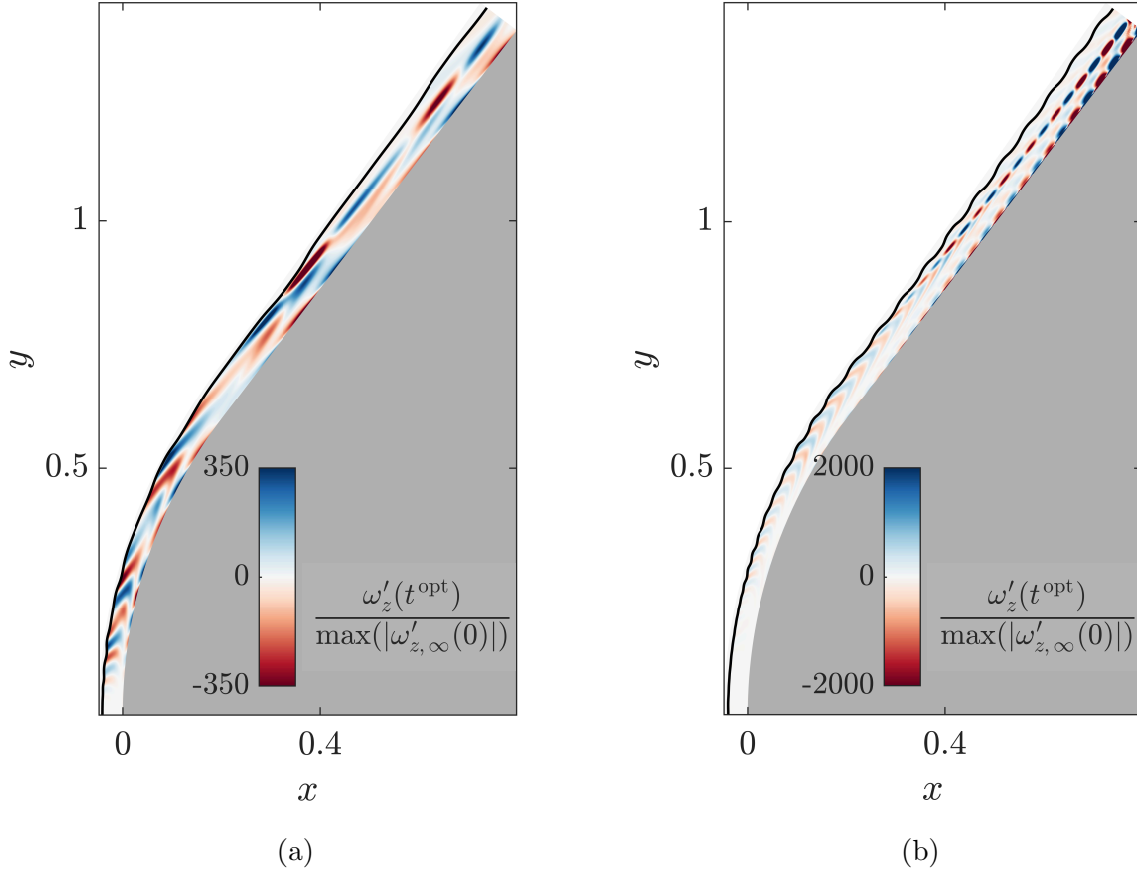


FIG. 18: Optimal disturbance that gives maximum steady-state energy growth  $G_T^{\text{opt}}$  for various Reynolds numbers  $Re_\infty$ . Base flow computed with freestream conditions from table I.  $M_\infty = 28.7$ . (a) Vorticity at the instant of peak gain on the limit cycle,  $Re_\infty = 20\,000$ . (b) Vorticity at the same instant,  $Re_\infty = 100\,000$ .

continues to be counteracted primarily by the pressure work associated with shock oscillations,  $\mathcal{T}_p^k$ . At higher Reynolds numbers, however, wave packets accumulate substantially more energy before exiting the computational domain. This is reflected in the advection term  $\mathcal{A}^k$ , which exhibits increasingly pronounced negative spikes at higher  $Re_\infty$  as energetic wave packets are advected out of the domain.

#### Appendix D: Kovásznyai reconstruction of the optimal freestream disturbance

The freestream-receptivity formulation in §II C 1 optimizes the incident perturbation only through its trace immediately upstream of the fitted bow shock. No upstream domain is solved, and no relation between the temporal frequency and the streamwise wavenumber is imposed during the optimization. The purpose of the present appendix is to describe the *a posteriori* reconstruction used to interpret the optimal shock trace as a superposition of Kovásznyai modes of the uniform freestream.

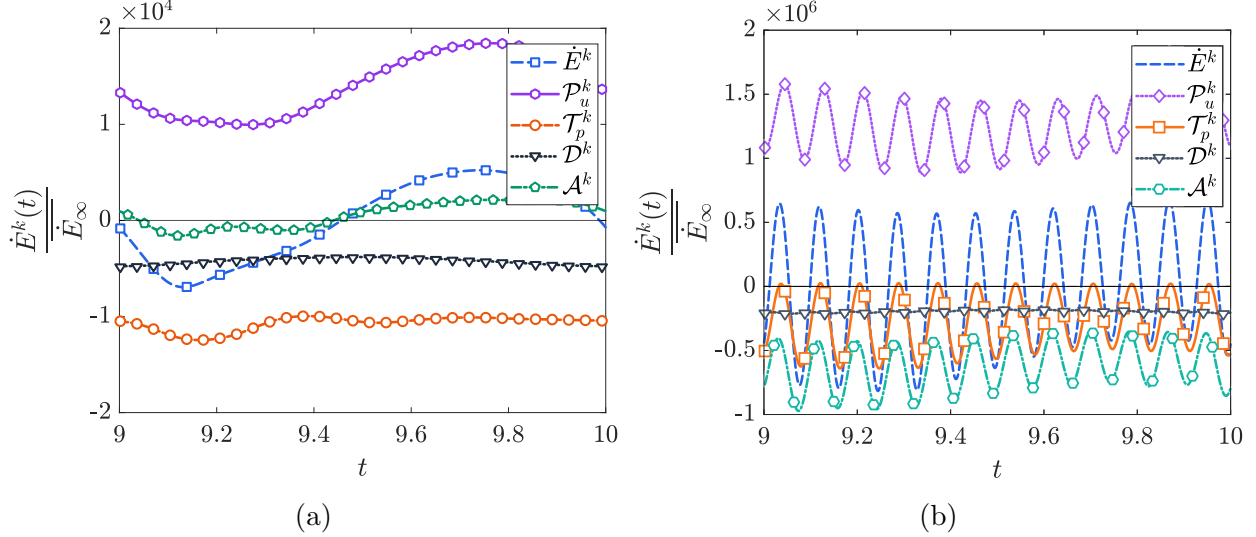


FIG. 19: Most important terms from the kinetic energy budget for the optimal disturbance that gives maximum energy growth  $G_T^{\text{opt}}$ . Budgets compared across two different Reynolds numbers  $Re_\infty = 20\,000$  and  $100\,000$ . Base flow computed with freestream conditions from table I.  $M_\infty = 28.7$ . Energy rates are non-dimensionalized with the mean freestream disturbance energy flux that crosses the shock wave,  $\dot{E}_\infty$ . Definitions and derivations of the budget terms are provided in Appendix B. (a) Kinetic energy budget,  $Re_\infty = 20\,000$ . (b) Kinetic energy budget,  $Re_\infty = 100\,000$ .

*a. Derivation of modes.* The uniform upstream flow is in the calorically perfect gas regime, with constant state  $(\rho_\infty, U_\infty, p_\infty, a_\infty, \gamma_\infty^*)$ , so that the freestream sound speed  $a_\infty$  and the Kovásznyai decomposition are well defined. We introduce coordinates aligned with the freestream,  $x_\parallel = \mathbf{e}_\parallel \cdot \mathbf{x}$  and  $x_\perp = \mathbf{e}_\perp \cdot \mathbf{x}$ , where  $\mathbf{e}_\parallel = \mathbf{u}_\infty / U_\infty$ . In the present reference frame, the  $x$ -axis is aligned with the freestream direction and the  $y$ -axis is the transverse direction, so that  $x_\parallel = x$ ,  $x_\perp = y$ ,  $u'_\parallel = u'$  and  $u'_\perp = v'$ . The Kovásznyai modes are written in the HYMOR/Chu variables

$$\boldsymbol{\psi}' = [p', u', v', S']^T, \quad S' = \frac{s'}{R_{g,\infty}},$$

using the plane-wave ansatz

$$\boldsymbol{\psi}'(\mathbf{x}, t) = \widehat{\boldsymbol{\psi}} \exp \{i(\alpha x_\parallel + \beta x_\perp - \omega t)\}, \quad (\text{D1})$$

where  $\alpha$  and  $\beta$  are the freestream-parallel and transverse wavenumbers,  $\mathbf{k} = \alpha \mathbf{e}_\parallel + \beta \mathbf{e}_\perp$  is the wavevector, and the Doppler-shifted frequency is  $\Omega = \omega - U_\infty \alpha$ .

In the uniform inviscid freestream, the entropy and vortical modes are convected with the mean flow, so  $\Omega = 0$  and hence  $\alpha_c = \omega / U_\infty$ . Writing  $K_c = (\alpha_c^2 + \beta^2)^{1/2}$  and  $\mathbf{k}_c = \alpha_c \mathbf{e}_\parallel + \beta \mathbf{e}_\perp$ ,

the entropic and vortical modes take the vector form

$$\mathbf{b}^e(\mathbf{x}, t; \omega, \beta) = \begin{bmatrix} 0 \\ 0 \\ 0 \\ 1 \end{bmatrix} \exp \{i(\alpha_c x_{\parallel} + \beta x_{\perp} - \omega t)\}, \quad (\text{D2})$$

$$\mathbf{b}^v(\mathbf{x}, t; \omega, \beta) = \begin{bmatrix} 0 \\ -\beta/K_c \\ \alpha_c/K_c \\ 0 \end{bmatrix} \exp \{i(\alpha_c x_{\parallel} + \beta x_{\perp} - \omega t)\}. \quad (\text{D3})$$

The first vector represents a pure convected entropy disturbance. The second has zero pressure and entropy perturbations and is solenoidal,  $\mathbf{k}_c \cdot \hat{\mathbf{u}} = 0$ .

The acoustic mode is isentropic, so the perturbation pressure and density obey the frozen sound-speed relation  $p' = a_{\infty}^2 \rho'$ . The linearized uniform-flow momentum and continuity equations then give

$$\rho_{\infty} \Omega \hat{\mathbf{u}} = \mathbf{k} \hat{p}, \quad \Omega^2 = a_{\infty}^2 (\alpha^2 + \beta^2).$$

Substituting  $\Omega = \omega - U_{\infty} \alpha$  into the dispersion relation, the acoustic values of  $\alpha$  for a prescribed pair  $(\omega, \beta)$  are the roots of

$$(U_{\infty}^2 - a_{\infty}^2) \alpha^2 - 2U_{\infty} \omega \alpha + (\omega^2 - a_{\infty}^2 \beta^2) = 0. \quad (\text{D4})$$

The pressure amplitude is normalized as  $\hat{p}^a = 1$ . For each acoustic root  $\alpha_{\pm}$  of (D4), with  $\Omega_{\pm} = \omega - U_{\infty} \alpha_{\pm}$ , the acoustic mode is

$$\mathbf{b}_{\pm}^a(\mathbf{x}, t; \omega, \beta) = \begin{bmatrix} 1 \\ \alpha_{\pm}/(\rho_{\infty} \Omega_{\pm}) \\ \beta/(\rho_{\infty} \Omega_{\pm}) \\ 0 \end{bmatrix} \exp \{i(\alpha_{\pm} x_{\parallel} + \beta x_{\perp} - \omega t)\}. \quad (\text{D5})$$

*b. Projection onto the bow shock.* The Kovásznyai modes of (D2)–(D5) are plane waves of the uniform freestream. The bow shock enters only as a curved locus of sampling points: each mode is a known function of the freestream-aligned coordinates  $(x_{\parallel}, x_{\perp})$ , and it is evaluated at the freestream-frame positions  $(x_{\parallel}(s_k), x_{\perp}(s_k))$  of the discrete shock stations  $s_k$ .

For each HYMOR frequency  $\omega_l$ , the optimized conservative-variable shock trace  $\hat{\mathbf{q}}_{\infty, l}^{\prime}(s_k)$  is first converted to the HYMOR/Chu variables  $\hat{\boldsymbol{\psi}}_l^H(s_k) = [\hat{p}, \hat{u}, \hat{v}, \hat{S}]^T$ . The Kovásznyai library is built directly from the mode templates of (D2)–(D5). We introduce the shock-evaluation operator  $\mathbf{b}_{k, l, m, r}$ , which samples the freestream plane wave of frequency  $\omega_l$ , transverse wavenumber  $\beta_m$ , and mode type  $r \in \{e, v, a_+, a_-\}$  at the  $N_s$  shock stations  $s_k$ ,

$$\mathbf{b}_{k, l, m, r} = \hat{\boldsymbol{\psi}}_{l, m, r} \exp \{i(\alpha_{l, m, r} x_{\parallel}(s_k) + \beta_m x_{\perp}(s_k))\}, \quad (\text{D6})$$

where  $\hat{\boldsymbol{\psi}}_{l, m, r}$  and  $\alpha_{l, m, r}$  are the eigenvector and freestream-parallel wavenumber carried by the chosen mode. The freestream-parallel wavenumber follows without any externally imposed dispersion assumption: the convected entropy and vortical modes take  $\alpha_c = \omega_l/U_{\infty}$ , while the two acoustic modes take the roots  $\alpha_{\pm}$  of the dispersion quadratic (D4).

Sweeping a set of transverse wavenumbers  $\{\beta_m\}_{m=1}^{N_\beta}$  and the mode types  $r$ , the fitted shock-trace variables are obtained as the contraction of the evaluation operator with the Kovásznyai coefficients  $c_{l,m,r}$ ,

$$\widehat{\psi}_l^K(s_k) = \sum_{m,r} \mathbf{b}_{k,l,m,r} c_{l,m,r}. \quad (\text{D7})$$

The coefficients are obtained from the weighted least-squares problem

$$c_{l,m,r} = \arg \min_{c_{l,m,r}} \sum_k \left| \mathbf{W}_l^{1/2}(s_k) \left( \mathbf{b}_{k,l,m,r} c_{l,m,r} - \widehat{\psi}_l^H(s_k) \right) \right|^2, \quad (\text{D8})$$

where the weight  $\mathbf{W}_l$  is the freestream Chu-energy flux weight used in the HYMOR input norm.

*c. Reconstruction of the freestream disturbance.* Once the coefficients  $c_{l,m,r}$  have been obtained from (D8), the same modes can be evaluated at any upstream point. Denoting by  $\widehat{\mathbf{b}}_{l,m,r}$  the eigenvector of the  $r$ th mode template carried by frequency  $\omega_l$  and transverse wavenumber  $\beta_m$  (with parallel wavenumber  $\alpha_{l,m,r}$ ), the reconstructed freestream disturbance is

$$\psi'_\infty(\mathbf{x}, t) = \Re \left\{ \sum_l \sum_m \sum_r c_{l,m,r} \widehat{\mathbf{b}}_{l,m,r} \exp [i (\alpha_{l,m,r} x_\parallel + \beta_m x_\perp - \omega_l t)] \right\}, \quad (\text{D9})$$

where  $r$  runs over the admissible mode types  $\{e, v, a_+, a_-\}$  retained for  $\beta_m$ . The quality of the reconstruction is measured by the captured energy fraction

$$\eta_{\text{cap}} = 1 - \frac{\sum_l (\widehat{\psi}_l^H - \widehat{\psi}_l^K)^\dagger \mathbf{W}_l (\widehat{\psi}_l^H - \widehat{\psi}_l^K)}{\sum_l (\widehat{\psi}_l^H)^\dagger \mathbf{W}_l \widehat{\psi}_l^H}, \quad (\text{D10})$$

where  $\widehat{\psi}_l^K$  is the fitted trace assembled from (D7). For the optimal disturbances discussed in §III A, the residual energy is negligible, so the upstream packet shown in figure 4 may be interpreted as the Kovásznyai extension of the HYMOR-optimized shock trace.

*d. Practical computation of the freestream projection.* The projection and reconstruction are performed through the following steps:

- Select the optimal HYMOR freestream-receptivity vector and extract the conservative-variable perturbation trace immediately upstream of the fitted bow shock for all retained frequencies.
- For each frequency  $\omega_l$ , reshape the extracted trace into the shock-station values  $\widehat{\mathbf{q}}_{\infty,l}(s_k)$  and convert it to the HYMOR/Chu variables  $\widehat{\psi}_l^H(s_k) = [\widehat{p}, \widehat{u}, \widehat{v}, \widehat{S}]^T$ .
- Compute the freestream-aligned coordinates  $x_\parallel(s_k)$  and  $x_\perp(s_k)$  of each shock station, which set the spatially varying phase of each plane wave along the curved shock (see above). Evaluate also the projected shock-area weights entering the Chu-energy flux inner product  $\mathbf{W}_l$ .
- For each swept transverse wavenumber  $\beta_m$  and mode type  $r \in \{e, v, a_+, a_-\}$ , evaluate the entry  $\mathbf{b}_{k,l,m,r}$  of the shock-evaluation operator (D6): the convected entropy and

vortical templates  $\mathbf{b}^e, \mathbf{b}^v$  use  $\alpha_c = \omega_l/U_\infty$ , while the acoustic templates  $\mathbf{b}_\pm^a$  are built from the real roots  $\alpha_\pm$  of the dispersion quadratic (D4) using the sound speed  $a_\infty$ .

- Solve the weighted least-squares problem (D8) for the coefficients  $c_{l,m,r}$ , where the fitted trace is the contraction  $\mathbf{b}_{k,l,m,r} c_{l,m,r}$  over the swept transverse wavenumbers  $m$  and mode types  $r$ .
- Reconstruct the optimal disturbance over the bow shock using  $\widehat{\psi}_l^K(s_k) = \mathbf{b}_{k,l,m,r} c_{l,m,r}$  from (D7), and evaluate the captured energy fraction (D10).
- Evaluate the same fitted Kovásznyai expansion away from the shock using (D9) to obtain the upstream freestream disturbance field implied by the optimal shock trace.